Partial Quantum Shadow Tomography for Structured Operators

A Thesis

submitted to
Indian Institute of Science Education and Research Pune
in partial fulfillment of the requirements for the
BS-MS Dual Degree Programme

by

Aniket Sengupta

Indian Institute of Science Education and Research Pune
Dr. Homi Bhabha Road,
Pashan, Pune 411008, INDIA.

April, 2025

Supervisor: T.S. Mahesh

Certificate

This is to certify that this dissertation entitled Partial Quantum Shadow Tomography for Structured Operators towards the partial fulfilment of the BS-MS dual degree programme at the Indian Institute of Science Education and Research, Pune represents study/work carried out by Aniket Sengupta at Indian Institute of Science Education and Research under the supervision of T.S. Mahesh, Professor, Department of Physics , during the academic year 2024-2025.

T.S. Mahesh

This thesis is dedicated to Maa and Baba

Declaration

I hereby declare that the matter embodied in the report entitled Partial Quantum Shadow Tomography for Structured Operators are the results of the work carried out by me at the Department of Physics, Indian Institute of Science Education and Research, Pune, under the supervision of T.S. Mahesh and the same has not been submitted elsewhere for any other degree.

Aniket Sengupta

Acknowledgments

First and foremost, I extend my deepest gratitude to my supervisor, Prof. T. S. Mahesh, for his unwavering guidance and support over the past two years. His mentorship has been instrumental in shaping my understanding of quantum information science and has provided me with invaluable insights into the world of research. Working under his supervision has not only deepened my appreciation for the subject but has also instilled in me the discipline and curiosity essential for scientific inquiry.

I am also immensely grateful to Prof. Sreejith G. J. for his invaluable contributions and insightful guidance throughout my thesis work. His suggestions and discussions have been crucial in refining my ideas and improving my research approach.

A special note of appreciation goes to Arijit Chatterjee for his significant help in my experimental work. His collaboration and support have made the research process both efficient and enjoyable. Working as a part of the NMR-QIP group has been a truly enriching experience, and I am thankful to my fellow group members—for their camaraderie, stimulating discussions, and the shared enthusiasm that made our time in the lab both productive and memorable.

Furthermore, I am deeply appreciative of my faculty mentor, Prof. Aparna Deshpande, for her continued encouragement and support. She has been one of the most responsive and approachable mentors, always willing to help with academic concerns and guide me through various aspects of my academic journey at IISER.

Beyond academics, I am profoundly grateful to my friends at IISER, who have been a pillar of support throughout my thesis year. Their encouragement, companionship, and the countless moments of joy we have shared have provided me with a strong sense of belonging.

The friendships and memories I have built here are something I will cherish for a lifetime.

Lastly, I would like to express my heartfelt gratitude to everyone who has contributed, directly or indirectly, to my academic and personal growth during this journey. This thesis would not have been possible without the collective support of my mentors, peers, and friends.

Abstract

Quantum shadow tomography based on the classical shadow representation provides an efficient way to estimate properties of an unknown quantum state without performing a full quantum state tomography. In scenarios where estimating the expectation values for certain classes of observables is required, obtaining information about the entire density matrix is unnecessary. We propose a partial quantum shadow tomography protocol, which allows estimation of a subset of the density matrix's elements contributing to the expectation values of certain classes of observables. This method utilizes tomographically incomplete subsets of single qubit Pauli basis measurements to perform partial tomography, making it experimentally more efficient. We have found a channel description allowing us to extract specific density matrix elements utilizing minimal sets of unitary applications. We demonstrate the advantage over unitary k designs such as Clifford and full Pauli by numerically analyzing the protocol for random states and different classes of observables. We experimentally demonstrate the partial estimation scheme for a wide class of two-qubit states (pure, entangled, and mixed) in the nuclear magnetic resonance (NMR) platform, which relies on ensemble-based measurements. The full density matrix re-constructed from different partial estimators produces fidelities exceeding 97%.

Contents

List of Figures

List of Tables

Chapter 1

Introduction

1.1 Density Matrix

In quantum mechanics, the state of a quantum system is mathematically represented by a density matrix. It provides a more general description of a system than a wave function, allowing for the representation of both pure and mixed states. The density matrix of a quantum system satisfies certain properties which are described below.

1. Trace: The Trace of a valid density matrix operator is always 1, $\mathrm{Tr}\{\rho\} = 1$.

2. Hermiticity: The density matrix is a Hermitian matrix, meaning $\rho = \rho^\dagger$, where $\rho^\dagger$ is the conjugate transpose of ρ.

3. Positivity: The density matrix is positive semi-definite, meaning all its eigenvalues are non-negative.

The density matrix formulation of quantum states effectively captures both quantum coherences (through off-diagonal elements) and statistical ensembles (via diagonal elements) associated with mixed states. It provides a unified description of pure and mixed states, accounting for both the phase relationships in superposition (coherences) and probabilistic mixtures of states.

1.2 Quantum State Tomography

Quantum state tomography is a process to reconstruct the full density matrix of a system based on experimental measurements. It involves determining the density matrix through a sequence of repeated measurements, generating the Born probabilities associated with each of the different basis measurements.

For a single qubit, common measurement bases include the Pauli operators (X, Y, Z). For multi-qubit systems, tensor products of these operators or Clifford group-based measurements are used. Methods such as linear inversion, maximum likelihood estimation (MLE), and compressed sensing help reconstruct the density matrix while ensuring physical constraints like positivity and unit trace. QST remains essential for quantum computing, cryptography, and experimental verification of quantum states.

However, the rapid growth of quantum platforms has exposed the limitations of traditional prediction techniques like quantum state tomography. This challenge arises from the curse of dimensionality, where the number of parameters needed to characterize a quantum system increases exponentially with the number of its components. Moreover, these parameters are not directly observable but must be inferred through measurements, which are both destructive—causing wavefunction collapse—and probabilistic, as dictated by Born's rule. Consequently, estimating even a single parameter with precision requires a large number of identically prepared quantum states. Additionally, the vast amount of measurement data must be processed and stored, demanding significant computational resources. In essence, fully reconstructing an n-qubit quantum state necessitates an exponential number of measurements, as well as exponential memory and computational power.

Quantum state tomography faces several limitations, making it impractical for large quantum systems. These drawbacks have led to the development of shadow tomography.

1. Exponential Scaling: The number of parameters in an n-qubit density matrix grows as 4^n, making reconstruction infeasible.

2. Large Measurement Overhead: Requires measurements in multiple bases, increasing exponentially with system size.

3. High Computational Cost: Reconstruction involves solving large optimization problems, demanding significant resources.
4. Noise Sensitivity: Susceptible to experimental errors, requiring complex corrections.
5. Redundant Information: Full state reconstruction is unnecessary when only expectation values are needed.
6. Storage and Post-Processing Issues: Handling large density matrices requires extensive memory and computation.

Quantum shadow tomography overcomes these issues by estimating expectation values directly, reducing measurement complexity and improving scalability.

Quantum shadow tomography is a more efficient alternative to quantum state tomography, particularly for large quantum systems. While quantum state tomography reconstructs the full density matrix, shadow tomography estimates expectation values of observables with significantly fewer measurements. It scales polynomially with the number of qubits, unlike state tomography, which scales exponentially.

- **Fewer measurements** – Uses randomized bases (Pauli/Clifford) instead of exhaustive measurements.
- **Better scalability** – Efficient for many-qubit systems.
- **Noise resilience** – Averaging reduces errors.
- **Task-specific efficiency** – Ideal for learning properties rather than full state reconstruction.

Shadow tomography is crucial in quantum information tasks, quantum verification, and near-term quantum technologies where quantum state tomography becomes infeasible.

1.3 Quantum Shadow Tomography

Quantum Shadow Tomography (QST) has emerged as an efficient way to estimate a wide range of properties of an unknown quantum state from the data collected via projective

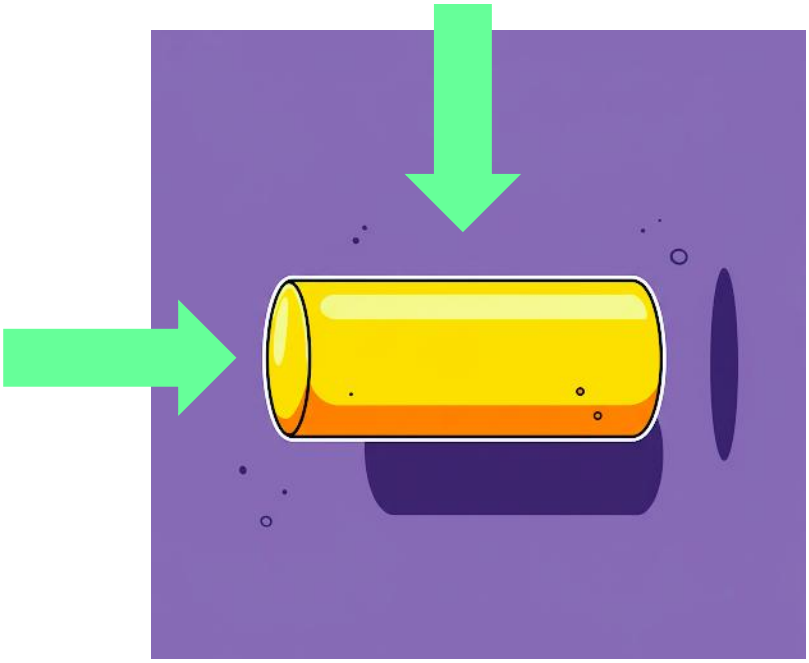

Figure 1.1: Shadow tomography: A pictorial analog of classical shadows constructed via quantum shadow tomography [17].

measurements on the state. QST was motivated by the seminal work of Aaronson [1], which established theoretical bounds for sampling complexity using Haar-random unitaries [27]. Subsequent advances introduced the classical shadow framework [19] which replaced Haar-random unitaries with simpler unitary designs, such as the Clifford group [34, 39] allowing for more efficient experimental implementation [31, 32] particularly on near-term quantum information devices in superconducting, trapped ions, and nuclear magnetic resonance (NMR) platforms.

The general QST protocol is outlined below. We perform a measurement procedure where we sample a unitary from the set $\zeta = \{U_i\}$ and apply it to the unknown state ρ, followed by a measurement in the computational basis $|k\rangle \in \{0,1\}^n$. The set of unitaries need to be sufficiently large that it is tomographically complete [19]- for any two distinct states, there should be at least one unitary $U \in \zeta$ and some computational basis state $b \in |k\rangle\langle k|$ such that the two states have different expectation values for $U^\dagger |b\rangle\langle b| U$. Full unitary group of Pauli basis measurements and the Clifford measurements are examples of such sets. The resulting collapsed state $|\hat{k}\rangle\langle\hat{k}|$ is reverse rotated using the inverse unitary $U_i^\dagger$

and the resulting outcome $U_i^\dagger|\hat{k}\rangle\langle\hat{k}|U_i$ is stored. We iterate this process

$$\rho \xrightarrow[\text{rotate}]{U_i} U_i\rho U_i^\dagger \xrightarrow[\text{Measure}]{} |\hat{k}\rangle\langle\hat{k}| \xrightarrow[\substack{\text{Inverse}\\ \text{rotate}}]{U_i^\dagger} U_i^\dagger|\hat{k}\rangle\langle\hat{k}|U_i \tag{1.1}$$

for different choices of unitaries and measurement outcomes. Now, if we average $U_i^\dagger|\hat{k}\rangle\langle\hat{k}|U_i$ over choices of unitary applications and measurement outcomes, we get a quantum channel map

$$\rho \to \mathcal{M}(\rho) = \mathbb{E}_{U,k}[U^\dagger|k\rangle\langle k|U] \approx \mathbb{E}_{i,\hat{k}}[U_i^\dagger|\hat{k}\rangle\langle\hat{k}|U_i] \tag{1.2}$$

where $\mathbb{E}_{U,k}$ is the weighted average over ζ and the computational basis states $|k\rangle$ weighted by Born probabilities, which can be estimated using the empirical average $\mathbb{E}_{i,\hat{k}}$ over both the sampled unitaries and the post measurement states $|\hat{k}\rangle$. The channel map has an inverse due to tomographic completeness of ζ [19]. The shadow estimator of the density matrix of the original state is given by the inverse channel map action on reverse rotated measurement outcomes, averaged over the sampling size

$$\widehat{\rho} = \mathbb{E}_{i,\hat{k}}[\mathcal{M}^{-1}(U_i^\dagger|\hat{k}\rangle\langle\hat{k}|U_i)], \tag{1.3}$$

Here $\widehat{\rho}$ is the shadow estimator, which in the limit of infinite shadows yields ρ [19]. If we know the inverse channel $\mathcal{M}^{-1}$, we can retrieve the density matrix ρ by taking an average over the classical shadows $\mathcal{M}^{-1}(U_i^\dagger|\hat{k}\rangle\langle\hat{k}|U_i)$. The quantum channel depends on the probability distribution over the unitary transformations. Sampling from the Haar measure (See Appendix A) over the full unitary group produces a depolarization channel (Appendix B) given by

$$\mathcal{D}_{1/2^n+1}(A) = \frac{A + \mathrm{Tr}(A)\mathbb{I}}{2^n + 1}. \tag{1.4}$$

The inverse channel is given by

$$\mathcal{D}^{-1}_{1/2^n+1}(A) = (2^n + 1)A - \mathrm{Tr}(A)\mathbb{I}. \tag{1.5}$$

The same quantum channel is generated when unitaries are sampled uniformly from the Clifford group $\mathrm{Cl}(2^n)$, consisting of $2^{n^2+2n}\prod_{j=1}^{n}(4^j - 1)$ unitaries for a n-qubit system.

Another tomographic complete set involves Pauli basis measurements, where the unitary

operator set takes the form $\zeta = \mathrm{Cl}(2)^{\otimes n}$. Effectively the protocol amounts to making a sequence of random measurements in x, y and z directions picked independently on each site. The shadow estimator formed by the Pauli basis measurements is given by

$$\widehat{\rho} = \mathbb{E}_{U \in \mathrm{Cl}(2)^{\otimes n}, \hat{k}} \left[\bigotimes_{j=1}^{n} \mathcal{D}_{1/3}^{-1}(U_j^\dagger \left| \hat{k_j} \right\rangle \left\langle \hat{k_j} \right| U_j) \right], \quad \text{where} \quad \hat{k}_1, \ldots, \hat{k}_n \in \{0, 1\} \tag{1.6}$$

In contrast to Clifford unitaries, Pauli basis measurements require only local control, with a significantly smaller set of unitaries.

1.4 Advances in Shadow Tomography

Classical shadows have found applications in quantum simulation tasks such as probing quantum scrambling [26, 12], in quantum machine learning tasks [14, 22], and vast usage in randomized measurement protocols for fidelity estimation, characterization of topological order [11], energy estimation [15], entanglement detection [10, 28] and many more. Subsequent advances introduced the classical shadow framework [19], replacing Haar-random unitaries with simpler unitary designs, such as the Clifford group [34, 39] allowing for more efficient experimental implementations [31, 32] particularly on near-term quantum devices. Apart from these two, other unitary ensembles which have been explored, include fermionic Gaussian unitaries [37], Pauli-invariant unitary ensembles [3], and unitary ensembles corresponding to time evolution of a random Hamiltonian [16]. Unitary ensembles defined through locally scrambled quantum dynamics [18] have been shown to achieve a lower tomography complexity compared to Clifford based methods. Recent developments in entangled-based measurements have shown a quadratic improvement in sampling complexity [21] to learn Pauli expectation values. Classical shadows using mutually unbiased bases (MUBs) [33] provide a framework for shadow tomography by measuring along $2^n + 1$ MUBs, ensuring a robust sampling complexity. The construction of MUB circuits, as detailed in [36], employs a $-cz - S - H-$ structure, enabling an efficient decomposition of each MUB circuit using $O(n^2)$ gates within $O(n^3)$ time. These advancements significantly reduce the required unitary samples and strive toward a systematic framework for efficient tomography.

Novel techniques in shadow tomography have been designed to mitigate the impact of experimental imperfections [7]. Neural networks have been used in combination with shadow tools for efficient quantum state reconstruction [35] that provides considerable advantages over direct shadow estimation. Its continued development focuses on optimizing protocols for scalability and noise resilience [20, 4, 38].

1.5 Motivation

In this work, we focus on scenarios where only partial information about an unknown state is needed. We propose partial quantum shadow tomography (PQST) that can efficiently extract expectation values for certain classes of observables. In the PQST protocol, unitaries are sampled from a tomographically incomplete set that does not form a full unitary design but suffices to extract relevant partial information about the unknown quantum state by focusing measurements on estimating specific density matrix elements. We also experimentally demonstrate PQST in nuclear magnetic resonance (NMR) system where PQST when combined with diagonal tomography of the ensemble system [2] can achieve accurate estimation of density matrix elements and thereby can achieve significant advantages over shadow protocols in these contexts.

Chapter 2

Partial Quantum Shadow Tomography

2.1 Estimation using subsets of tomographically complete unitaries

QST provides full characterization of a quantum state and involves sampling unitaries from a tomographically complete set. This in principle allows for the estimation of any observable and can be extended to quantities non-linear in the density matrix such as the subsystem entropies. In this work, we consider the task of estimating expectation values of observables which are Pauli strings $\{\mathbb{I}, X, Y, Z\}^{\otimes n}$, using shadow tomography with optimally chosen unitaries. We investigate whether sampling unitaries from subsets of a tomographically complete set still permits partial state reconstruction via the pseudo-inverse map:

$$\mathcal{M}_p^{-1}(A) = pA - \mathbb{I}, \tag{2.1}$$

where p is the strength of the pseudo-inverse map. This map is not completely positive and trace-preserving. However, when $p = 2^n + 1$, it acts as an inverse depolarizing map that preserves the trace for states with $\mathrm{Tr}(A) = 1$, though it remains non-completely positive. It is called the pseudo-inverse because it serves as the inverse only for a subset of density matrix elements, enabling the selective estimation of those elements, as described in the following sections.

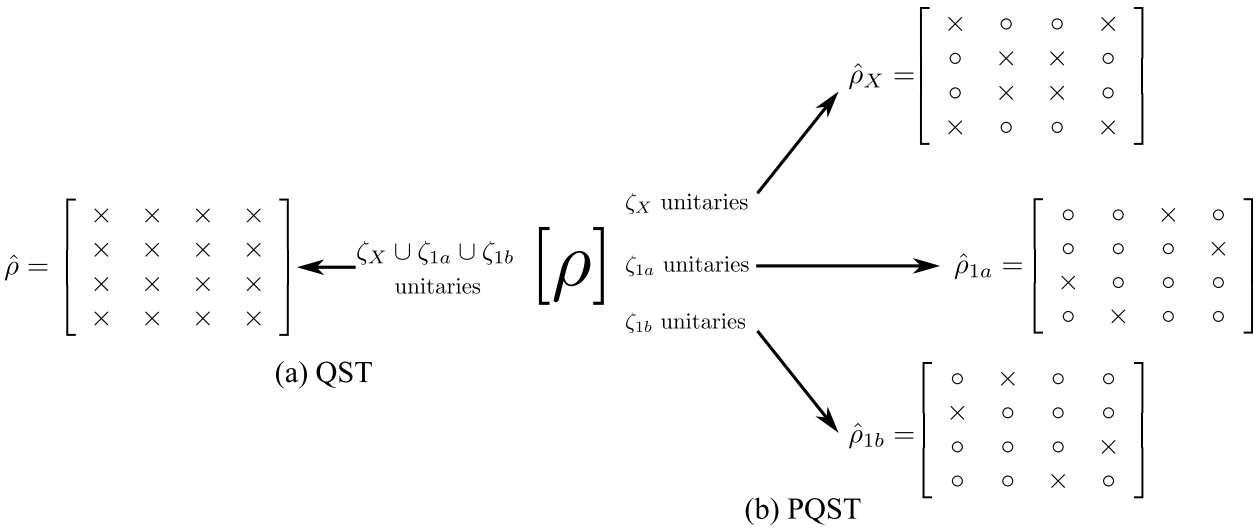

Figure 2.1: Illustrating (a) QST- full state characterization by sampling unitaries from tomographic completer set of unitaries and (b) PQST-partial characterization by sampling unitaries from a subset of Clifford unitary design, on a 2-qubit system. In each partial shadow estimator $\widehat{\rho}_i$, the density matrix elements represented by $\{\times\}$ are efficiently estimated in the PQST protocol, while the elements represented by $\{\circ\}$ are discarded. However, by combining multiple partial shadow estimators $\{\widehat{\rho}_i\}$, the full density matrix is reconstructed, as described in Eqn. (2.12).

More precisely, we aim to determine suitable combinations of triplets $\{p, \zeta', \mathcal{O}\}$, where p is the strength of the pseudo-inverse map $\mathcal{M}_p^{-1}(\cdot)$ defined in Eq. (2.1), ζ' is a subset of the tomographically complete set ζ with $\mathcal{O}$ is the set of observables of Pauli string type, such that the shadow estimator $\widehat{\rho}$ constructed using unitaries U_i uniformly sampled from ζ', given by

$$\widehat{\rho} = \mathbb{E}_{i,\hat{k}} \left[\mathcal{M}_p^{-1} \left(U_i^\dagger \left| \hat{k} \right\rangle \left\langle \hat{k} \right| U_i \right) \right]. \tag{2.2}$$

satisfies the following relation:

$$\langle O \rangle_\rho = \mathrm{Tr}(O\widehat{\rho}). \tag{2.3}$$

for some non-trivial set of Pauli string observables $O \in \mathcal{O}$.

To illustrate this idea, we consider a two-qubit system ρ, where we sample specific subsets of unitaries from $\zeta = \mathrm{Cl}(2)^{\otimes 2}$ and construct $\widehat{\rho}$ using the pseudo-inverse map $\mathcal{M}_p^{-1}(\cdot)$. At first, we take the unitary set consisting of only one unitary $\zeta' = \{\mathbb{I} \otimes \mathbb{I}\}$, we generate the

shadow estimator, which in the limit of a large number of samples reduces to

$$\widehat{\rho}_{\mathbb{I}\otimes\mathbb{I}} = p\ \mathrm{diag}(\rho) - \mathbb{I}, \quad \text{where} \quad \mathrm{diag}(\rho) = (\rho_{00,00} \quad \rho_{01,01} \quad \rho_{10,10} \quad \rho_{11,11}) \tag{2.4}$$

In general, it does not estimate any non-trivial Pauli string observable except $\mathbb{I}\otimes\mathbb{I}$ when $p = 5$. None of the other density matrix elements can be recovered. Consequently, additional post-processing is required to estimate observables such as $\mathbb{I}\otimes Z$, $Z\otimes\mathbb{I}$, $Z\otimes Z$. Now we explore other cases: $\zeta' = \{H\otimes H\}$ and $\zeta' = \{HS\otimes HS\}$, for which the estimator in Eq. 2.2 approaches $\widehat{\rho}_{H\otimes H}$ and $\widehat{\rho}_{HS\otimes HS}$ respectively, given by

$$\widehat{\rho}_{H\otimes H} = -\mathbb{I} + \frac{p}{4}\mathcal{B}_H. \tag{2.5}$$

$$\widehat{\rho}_{HS\otimes HS} = -\mathbb{I} + \frac{p}{4}\mathcal{B}_{HS}. \tag{2.6}$$

The explicit form of $\mathcal{B}_H$ and $\mathcal{B}_{HS}$ matrices are given in the Appendix C in Eqns. (C.7) and (C.9) respectively. These estimators fail to accurately estimate any non-trivial Pauli string observables for any values of p. As further examples, for $\zeta' = \{\mathbb{I}\otimes\mathbb{I}, H\otimes H\}$, and $\zeta' = \{\mathbb{I}\otimes\mathbb{I}, HS\otimes HS\}$ we generate the estimator using Eq. (2.2) which approaches $\widehat{\rho}_{\mathbb{I},H}$ and $\widehat{\rho}_{\mathbb{I},HS}$

$$\widehat{\rho}_{\mathbb{I},H} = -\mathbb{I} + \frac{p}{8}\mathcal{B}_H + \frac{p}{2}\ \mathrm{diag}(\rho). \tag{2.7}$$

$$\widehat{\rho}_{\mathbb{I},HS} = -\mathbb{I} + \frac{p}{8}\mathcal{B}_{HS} + \frac{p}{2}\ \mathrm{diag}(\rho). \tag{2.8}$$

The estimators $\widehat{\rho}_{\mathbb{I},H}$ and $\widehat{\rho}_{\mathbb{I},HS}$ again fail to estimate any non-trivial Pauli string observables for any p values. These examples suggest that arbitrary subsets of ζ for any p-values cannot be used to easily estimate expectation values of any nontrivial Pauli string observables. However, an explicit scan through all the subsets suggests a convenient set of unitaries which satisfy the above requirements can be found to be

$$\zeta_X = \{\mathbb{I}\otimes\mathbb{I}, H\otimes H, H\otimes HS, HS\otimes H, HS\otimes HS\}$$

$$\zeta_1 = \{\mathbb{I}\otimes\mathbb{I}, H\otimes\mathbb{I}, \mathbb{I}\otimes H, \mathbb{I}\otimes HS, HS\otimes\mathbb{I}\}.$$

The estimator Eq (2.2) with $p = 5$, and unitaries sampled from ζ_X and ζ_1 approach $\widehat{\rho}_X$ and

$\widehat{\rho}_1$ respectively and are given by:

$$\widehat{\rho}_X = \begin{pmatrix} \rho_{00,00} & \rho_{00,01} + \rho_{10,11} & \rho_{00,10} + \rho_{01,11} & \rho_{11,11} \\ \rho_{01,00} + \rho_{11,10} & \rho_{01,01} & \rho_{01,10} & \rho_{01,11} + \rho_{00,10} \\ \rho_{10,00} + \rho_{11,01} & \rho_{10,01} & \rho_{10,10} & \rho_{10,11} + \rho_{00,01} \\ \rho_{00,11} & \rho_{11,01} + \rho_{10,00} & \rho_{11,10} + \rho_{01,00} & \rho_{11,11} \end{pmatrix} \tag{2.9}$$

$$\widehat{\rho}_1 = \begin{pmatrix} 2\rho_{00,00} - \rho_{11,11} & \rho_{00,01} & \rho_{00,10} & 0 \\ \rho_{01,00} & 2\rho_{01,01} - \rho_{10,10} & 0 & \rho_{01,11} \\ \rho_{10,00} & 0 & 2\rho_{10,10} - \rho_{01,01} & \rho_{10,11} \\ 0 & \rho_{11,01} & \rho_{11,10} & 2\rho_{11,11} - \rho_{00,00} \end{pmatrix} \tag{2.10}$$

The estimator $\widehat{\rho}_X$ accurately captures the diagonal and anti-diagonal elements of the density matrix. The other remaining off-diagonal elements are captured in their respective positions via the estimator $\widehat{\rho}_1$.

Note that $\widehat{\rho}_X$ allows to calculate, without any additional processing, the expectation values of Pauli strings $\mathcal{O}_X = \{\mathbb{I}\otimes\mathbb{I},\ \mathbb{I}\otimes Z,\ Z\otimes\mathbb{I},\ Z\otimes Z,\ X\otimes X,\ Y\otimes Y,\ X\otimes Y,\ X\otimes Y\}$ and their arbitrary linear combinations. These operators set includes widely studied models such as the XYZ Hamiltonian with longitudinal field and therefore can be useful in efficient use of shadow tomography approaches for variational quantum algorithms on such Hamiltonians. On the other hand, the estimator $\widehat{\rho}_1$ allows one to calculate the expectation values of the Pauli strings $\mathcal{O}_1 = \{\mathbb{I}\otimes X,\ \mathbb{I}\otimes Y,\ X\otimes\mathbb{I},\ Y\otimes\mathbb{I},\ X\otimes Z,\ Y\otimes Z,\ Z\otimes X,\ Z\otimes X\}$ and their arbitrary linear combinations via Eqn. (2.3). Combining the two estimates allows complete characterization of the density matrix. More importantly, if the observables to be estimated are in either of the sets, estimation can be performed more efficiently than full shadow tomography.

The structure of the subsets ζ_X and ζ_1 can be generalized by carefully tuning $p-$values to get similar efficient estimates of larger Pauli strings inside a general n-qubit system. We discuss this in Sec. 2.7. Lastly we note that the unitary set $\zeta = \{\mathbb{I}, H, HS\}^{\otimes n}$ is also a subset of Pauli basis measurements $\zeta \subset \mathrm{Cl}(2)^{\otimes n}$. However, we find that when the inverse channel description from the Pauli basis measurements given in the Eqn. (1.6) is used in conjugation

with ζ_X, we do not recover correct matrix elements without using correction factors.

2.2 Partial Quantum Shadow Tomography Protocol

The PQST protocol [29] involves performing independent shadow tomography using different sets of unitaries $\zeta_1, \zeta_2, \ldots$, where each set ζ_i is associated with an pseudo-inverse map described in Eq. (2.1) for some appropriate strength $p_1, p_2, \ldots$, yielding Partial Shadow Estimators (PSEs) $\widehat{\rho}_1, \widehat{\rho}_2, \ldots$

$$\begin{aligned} \zeta_1, p_1 : \rho &\xrightarrow{QST} \widehat{\rho}_1 \\ \zeta_2, p_2 : \rho &\xrightarrow{QST} \widehat{\rho}_2 \\ \zeta_3, p_3 : \rho &\xrightarrow{QST} \widehat{\rho}_3 \\ &\vdots \end{aligned} \tag{2.11}$$

Each PSE captures partial disjoint pieces of information about the quantum state. As shown in Sec. 2.7, these PSEs collectively reconstruct the full density matrix by:

$$\rho = \sum_{i=1}^{N} \mathcal{P}_i(\widehat{\rho}_i), \tag{2.12}$$

where $\mathcal{P}_i(\cdot)$ projects the density matrix elements which preserves those elements that each estimator $\widehat{\rho}_i$ can estimate. This process is illustrated in Fig. 2.1.

Here, we introduce the active notation for density matrix elements [25]. Let ρ be the density matrix of an n-qubit quantum system, expressed in the computational basis $\{|k\rangle\}_{k=0}^{2^n-1}$. The matrix element ρ_{ij} corresponds to the transition amplitude between the basis states $|i\rangle$ and $|j\rangle$, i.e., $\rho_{ij} = \langle i|\rho|j\rangle$. Here, i and j are bit strings of length n, representing the computational basis states $|i\rangle$ and $|j\rangle$ of the n-qubit system, given by the tensor product of single-qubit basis states. A matrix element ρ_{ij} is said to be d-active if the bit strings i and j differ in exactly d sites. This difference is quantified by the Hamming distance, which counts the number of positions where i and j have different bits.

2.3 PQST in ensemble systems

In the context of ensemble systems like in NMR, PQST can be implemented efficiently by measuring population elements via diagonal tomography, which is equivalent to performing a large number of projective measurements [2, 24, 30]. In this case, averaging over computational basis states $|k\rangle$ is captured by diagonal tomography. Given a quantum state ρ encoded in an ensemble quantum processor, the PQST is realized via the following steps:

(i) First rotate the target state ρ under $U_i \in \zeta$, i.e., $\rho \to U_i \rho U_i^\dagger$.

(ii) Readout all the diagonal elements $\left\langle k \left| U_i \rho U_i^\dagger \right| k \right\rangle = P_{ik}$ by performing diagonal tomography in the computational basis $\{|k\rangle\}$.

(iii) Reverse rotate the diagonal state on a classical processor to obtain the given matrix

$$\sum_k U_i^\dagger \left(P_{ik} |k\rangle\langle k| \right) U_i \tag{2.13}$$

(iv) Average over the choices of unitary and invert using the pseudo-inverse map of Eq. (2.1) to construct the PSE

$$\widehat{\rho}_\zeta = E_{U_i \in \zeta} \left[\mathcal{M}_p^{-1} \left(\sum_k U_i^\dagger \left(P_{ik} |k\rangle\langle k| \right) U_i \right) \right]. \tag{2.14}$$

In the following, we consider PQST for quantum registers of different sizes.

2.4 Shadow protocol for 1-qubit system

Using the uniform sampling of unitaries from set $\zeta = \{\mathbb{I}, H, HS\}$, the full shadow estimator can be written as

$$\widehat{\rho} = \mathbb{E}_{\hat{k}, U_i \in \zeta} \left[\mathcal{M}_3^{-1} \left(U_i^\dagger \left| \hat{k} \right\rangle \left\langle \hat{k} \right| U_i \right) \right], \tag{2.15}$$

where $\left| \hat{k} \right\rangle$ is the measurement outcome in the computational basis $|k\rangle$ after rotating ρ with U_i. It requires only three unitaries for the full density matrix estimation without any ap-

proximation in the large measurement limit. Here, we used the channel strength $p = 3$ for the pseudo-inverse (2.1).

2.4.1 Proof

We will analyze the tomographically complete set of unitaries for a single qubit and extend these insights to multi-qubit systems. The most general density matrix for a single qubit is given by

$$\rho = \frac{1}{2}\left(I + r_x X + r_y Y + r_z Z\right). \tag{2.16}$$

Measurement after $U_1 = I$ The measurement outcomes $p(0)$ and $p(1)$ are given by:

$$p(0) = \langle 0|\rho|0\rangle = \frac{1}{2}\left(1 + r_z\right), \tag{2.17}$$

$$p(1) = \langle 1|\rho|1\rangle = \frac{1}{2}\left(1 - r_z\right). \tag{2.18}$$

Measurement after $U_2 = H$ The Hadamard gate H transforms ρ to $H\rho H^\dagger$.

$$p(0) = \langle 0|H\rho H^\dagger|0\rangle = \frac{1}{2}\left(1 + r_x\right), \tag{2.19}$$

$$p(1) = \langle 1|H\rho H^\dagger|1\rangle = \frac{1}{2}\left(1 - r_x\right). \tag{2.20}$$

Measurement after $U_3 = HS$ The combination HS transforms ρ to $HS\rho(HS)^\dagger$.

$$p(0) = \langle 0|HS\rho(HS)^\dagger|0\rangle = \frac{1}{2}\left(1 - r_y\right), \tag{2.21}$$

$$p(1) = \langle 1|HS\rho(HS)^\dagger|1\rangle = \frac{1}{2}\left(1 + r_y\right). \tag{2.22}$$

Now, the Eqns (2.19)-(2.22), specify that the set of unitaries $(U_1 = I, U_2 = H, U_3 = HS)$ forms a tomographically complete set for the case of a single qubit.
The difference in the r_z values between two different states is captured by $U_1 = I$, similarly the difference in the r_x values between two different states is captured by $U_1 = H$ and the

difference in the r_y values between two different states is captured by $U_1 = HS$.
I will demonstrate with some examples and pictorial representation for the case of a single qubit.

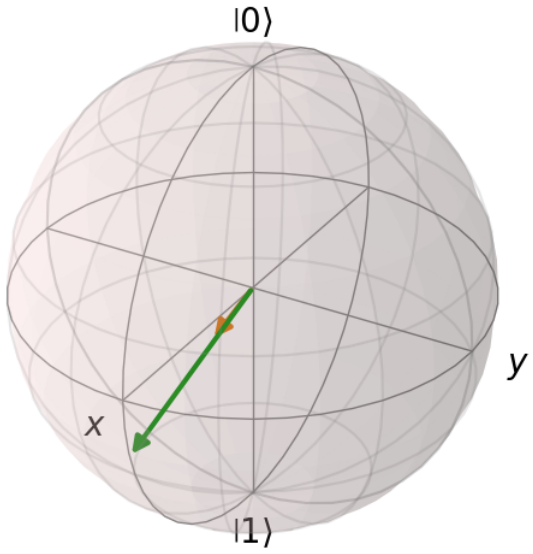

Figure 2.2: Quantum State (Green) and the Depolarizing Channel (orange) visualization.

2.5 PQST of a 2-qubit system

For the 2-qubit case, the full tomography complete set consists of all tensor products of the single qubit unitaries, i.e., $\{\mathbb{I}, H, HS\}^{\otimes 2}$, which has 9 unitaries. We can divide these unitaries into two sets

$$\zeta_X = \{\mathbb{I} \otimes \mathbb{I}, H \otimes H, H \otimes HS, HS \otimes H, HS \otimes HS\}$$

The shadow estimator $\widehat{\rho}_X$ generated from ζ_X with $p = 5$, estimates zero-active (diagonal) and two-active (anti-diagonal) elements of a 2-qubit density matrix.

	$\langle 00\vert$	$\langle 01\vert$	$\langle 10\vert$	$\langle 11\vert$
$\vert 00\rangle$	$\rho_{00,00}$	$\rho_{00,01}$	$\rho_{00,10}$	$\rho_{00,11}$
$\vert 01\rangle$	$\rho_{01,00}$	$\rho_{01,01}$	$\rho_{01,10}$	$\rho_{01,11}$
$\vert 10\rangle$	$\rho_{10,00}$	$\rho_{10,01}$	$\rho_{10,10}$	$\rho_{10,11}$
$\vert 11\rangle$	$\rho_{11,00}$	$\rho_{11,01}$	$\rho_{11,10}$	$\rho_{11,11}$

Table 2.1: Two-qubit PQST using sets ζ_X and ζ_1 of Sec. 2.5, which extract PSEs $\widehat{\rho}_X$ estimating diagonal and anti-diagonal elements represented by dashed boxes and $\widehat{\rho}_1$ estimating the other off-diagonal elements represented by solid boxes, respectively. The channel description is provided in Appendix C.

$$\zeta_1 = \{\mathbb{I}\otimes\mathbb{I}, H\otimes\mathbb{I}, \mathbb{I}\otimes H, \mathbb{I}\otimes HS, HS\otimes\mathbb{I}\}$$

The shadow estimator $\widehat{\rho}_1$ generated from ζ_1 with $p = 5$, estimates all the single-active elements of a 2-qubit density matrix. Further $\zeta_1 = \zeta_{1a} \cup \zeta_{1b}$ can be further separated into two subsets.

(i) $\zeta_{1a} = \{\mathbb{I}\otimes\mathbb{I}, H\otimes\mathbb{I}, HS\otimes\mathbb{I}\}$ with $p = 3$, yields PSE $\widehat{\rho}_{1a} = \{\rho_{00,10}, \rho_{01,11}, \rho_{10,00}, \rho_{11,01}\}$ estimating single-active terms of the first qubit.

(ii) $\zeta_{1b} = \{\mathbb{I}\otimes\mathbb{I}, \mathbb{I}\otimes H, \mathbb{I}\otimes HS\}$ with $p = 3$, yields PSE $\widehat{\rho}_{1b} = \{\rho_{00,01}, \rho_{01,00}, \rho_{10,11}, \rho_{11,10}\}$ estimating single-active terms of the second qubit.

The reconstructed channel description for each set of unitaries is analyzed in Appendix C.

2.6 PQST for a 3-qubit system

The full unitary set $\{\mathbb{I}, H, HS\}^{\otimes 3}$ can be divided into three sets (Fig. 2.3)

(i) The unitary set $\zeta_X = \{\mathbb{I}^{\otimes 3}, u_1\otimes u_2\otimes u_3\}$, where $u_i \in \{H, HS\}$, consists of unitaries that apply either the identity operation or a non-identity unitary (H or HS) across

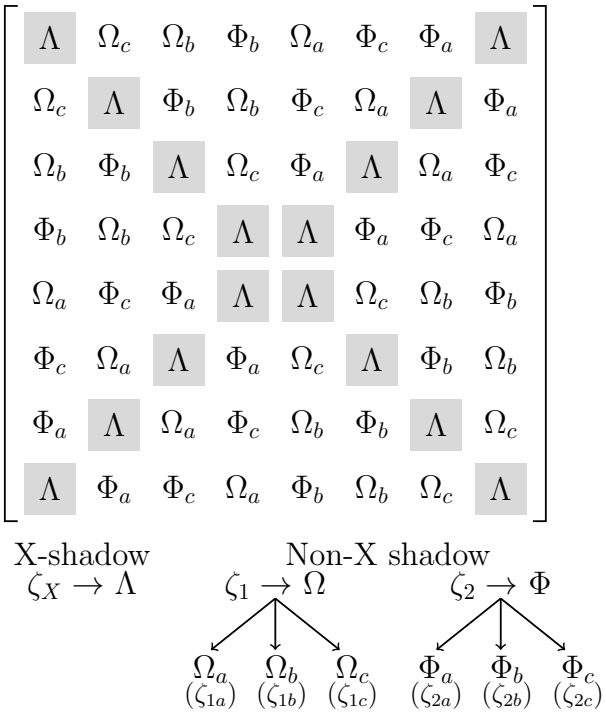

Figure 2.3: PQST of a 3-qubit system. The estimator $\widehat{\rho}_X$, generated by ζ_X, efficiently estimates the density matrix elements corresponding to the Λ positions of the X-shadow, while the estimators $\widehat{\rho}_1$ and $\widehat{\rho}_2$, generated by ζ_1 and ζ_2, respectively, efficiently estimate the single-active terms Ω and double-active terms Φ. Ω and Φ can be further divided into subsets as mentioned in Sec. 2.6.

all three qubits. This set includes a total of 9 unitaries. The PSE $\widehat{\rho}_X$ constructed by uniformly sampling unitaries from this set estimates the diagonal (0-active) and anti-diagonal (3-active) elements of the density matrix, denoted by Λ in Fig. 2.3. The reconstruction is performed using the pseudo-inverse transformation in Eq. (2.1) with an associated channel strength of $p = 9$.

(ii) $\zeta_1 = \{\mathbb{I}^{\otimes 3},\ u_1 \otimes \mathbb{I} \otimes \mathbb{I}, \mathbb{I} \otimes u_2 \otimes \mathbb{I}, \mathbb{I} \otimes \mathbb{I} \otimes u_3\}$ consists of unitaries where non-identity unitaries $u_i \in \{H, HS\}$ act only on a single site. This set contains a total of 7 unitaries. The PSE $\widehat{\rho}_1$, constructed by uniformly sampling unitaries from this set, estimates the single-active terms (labeled as Ω in Fig. 2.3) of the density matrix. The reconstruction follows the pseudo-inverse transformation in Eq. (2.1), with an associated channel strength of $p = 7$. It can be further divided into the following subsets

$\zeta_{1a} = \{\mathbb{I}^{\otimes 3}, u_1 \otimes \mathbb{I} \otimes \mathbb{I}\}$ is used to construct the PSE $\widehat{\rho}_{1a}$, which estimates the single-active terms of the first qubit, denoted by Ω_a in Fig, 2.3. The reconstruc-

tion follows the pseudo-inverse transformation (2.1) with an associated channel strength of $p = 3$.

$\zeta_{1b} = \{\mathbb{I}^{\otimes 3}, \mathbb{I} \otimes u_2 \otimes \mathbb{I}\}$ is used to construct the PSE $\widehat{\rho}_{1b}$, which estimates the single-active terms of the second qubit, denoted by Ω_b in Fig, 2.3 with an associated channel strength of $p = 3$.

$\zeta_{1c} = \{\mathbb{I}^{\otimes 3}, \mathbb{I} \otimes \mathbb{I} \otimes u_3\}$ is used to construct the PSE $\widehat{\rho}_{1b}$, which estimates the single-active terms of the third qubit, denoted by Ω_c in Fig. 2.3 with an associated channel strength of $p = 3$.

Note that each of these subsets ζ_{1i} consists of three unitaries. The terms estimated from each subset correspond to the active terms of the qubit on which the applied unitary is non-identity. To estimate the single-active terms of the first and second qubits, we combine the subsets as $\zeta_{1ab} = \zeta_{1a} \cup \zeta_{1b}$, (consisting of five unitaries) with the channel strength parameter set to $p = 5$ for reconstruction, which we find by inspection. This approach can be extended to different combinations of subsets.

(iii) $\zeta_2 = \{\mathbb{I}^{\otimes 3},\ u_1 \otimes u_2 \otimes \mathbb{I}, \mathbb{I} \otimes u_2 \otimes u_3, u_1 \otimes \mathbb{I} \otimes u_3\}$ consists of unitaries where the non-identity unitaries $u_i \in \{H, HS\}$. This set contains a total of 13 unitaries. The PSE $\widehat{\rho}_2$, constructed by uniformly sampling unitaries from this set, estimates the two-active terms (labelled as Φ in Fig. 2.3) of the density matrix. The reconstruction follows the pseudo-inverse transformation in Eq. (2.1), with an associated channel strength of $p = 13$. It can be further divided into the following subsets

$\zeta_{2a} = \{\mathbb{I}^{\otimes 3}, u_1 \otimes u_2 \otimes \mathbb{I}\}$ constructs the PSE $\widehat{\rho}_{2a}$, which estimates the 2-active terms of the first and second qubit, denoted as Φ_a in Fig. 2.3 using the pseudo-inverse map (2.1) with strength parameter $p = 5$.

$\zeta_{2b} = \{\mathbb{I}^{\otimes 3}, \mathbb{I} \otimes u_2 \otimes u_3\}$ constructs the PSE $\widehat{\rho}_{2b}$, which estimates the 2-active terms of the first and second qubit,, denoted as Φ_b in Fig. 2.3 with strength parameter $p = 5$.

$\zeta_{2c} = \{\mathbb{I}^{\otimes 3}, u_1 \otimes \mathbb{I} \otimes u_3\}$ constructs the PSE $\widehat{\rho}_{2c}$, which estimates the 2-active terms of the first and second qubit, denoted as Φ_c in Fig. 2.3 with strength parameter $p = 5$.

Each of these subsets consists of five unitaries with $p = 5$. By combining the subsets ζ_{2a} and ζ_{2b}, we define $\zeta_{2ab} = \zeta_{2a} \cup \zeta_{2b}$, which consists of 9 unitaries. We construct

the estimator by uniform sampling of unitaries from $\zeta + 2ab$ with channel strength $p = 9$ (2.1), allowing us to estimate 2-active terms of the density matrix where qubits 1 and 2 are active, as well as where qubits 2 and 3 are active, simultaneously.

Through these examples, it becomes evident that the strength of the pseudo-inverse is equal to the cardinality of the corresponding unitary set ζ, given by $p = |\zeta|$. This protocol allows to generate PSEs (2.2) which estimate the elements of the density matrix that belong to particular active orders.

2.7 Generalized PQST Protocol

For an n-qubit system, the full unitary set is given by 3^n unitary operations $\zeta = \{\mathbb{I}, H, HS\}^{\otimes n}$. We consider the question of estimating the A-active matrix elements of ρ for which qubits in a subset A of the set of all qubits are active. For this, we introduce a set of unitary ζ_A containing, in addition to $\mathbb{I}^{\otimes n}$ the unitaries that act trivially on the complement of A and as non-trivial $u \in \{H, HS\}$ unitaries on the qubits in A. Set ζ_A enables the estimation of all A-active terms of the density matrix using the estimator in Eq. (2.2) and the pseudo-inverse map Eq. (2.1) with $p = |\zeta_A| = 2^{|A|} + 1$, where $|.|$ denotes the cardinality.

We empirically find that the idea can be extended to simultaneously calculate all A active and B active density matrix elements for two subsets A and B of same cardinality. For this we use the set $\zeta_A \cup \zeta_B$ and use the estimator (2.2) with the pseudo-inverse map with $p = |\zeta_A \cup \zeta_B|$. This can be generalized to a combination of more subsets $A_1, A_2 \ldots$ all of the same size. For instance all the m-active elements ($1 \leq m \leq n$) of ρ can be calculated using a unitary set of size $p = \binom{n}{m} \times 2^m + 1$.

To be more precise, we have outlined the protocol for a n-qubit system

(i) $\zeta_X = \left\{\mathbb{I}^{\otimes n}, \bigotimes_{i=1}^{n} u_i\right\}$, where $u_i \in \{H, HS\}$. This set has $2^n + 1$ elements and the corresponding PSE $\widehat{\rho}_X$ is generated using the pseudo-inverse Eq. (2.1) with $p = |\zeta_X| = 2^n + 1$. $\widehat{\rho}_X$ estimates the X-shadow (Fig. 2.3), i.e., zero-flip (diagonal) and n-flip (anti-diagonal) elements of the density matrix.

(ii) $\zeta_1 = \{\mathbb{I}^{\otimes n}, \{\eta_\alpha\}\}$ with $\alpha \in [1, 2, \cdots, n]$, $\eta_\alpha = \left\{\bigotimes_{i=1}^{n} u_i\right\}$, and $u_{i=\alpha} \in \{H, HS\}$ and

$u_{i\neq\alpha} = \mathbb{I}$. This set contains $2n+1$ unitaries. The PSE ζ_1 is generated via sampling these unitaries and applying the inverse map (2.1) with $p = |\zeta_1| = 2n+1$. The estimator $\widehat{\rho}_1$ estimates all the single-flip elements, while the PSE $\widehat{\rho}_{1\alpha}$, corresponding to the subset $\zeta_{1\alpha} = \{\mathbb{I}^{\otimes n}, \eta_\alpha\}$, estimates elements corresponding to the single-flip of the α-th qubit, with $p = |\zeta_{1\alpha}| = 3$. Subsequently, we can combine different subsets, $\tilde{\zeta}_1 = \bigcup_i \zeta_{1i}$, and estimate the corresponding single-flip terms using $p = |\tilde{\zeta}_1|$.

(iii) $\zeta_d = \{\mathbb{I}^{\otimes n}, \{\eta_{\alpha_1\cdots\alpha_d}\}\}$ for distinct $\alpha_k \in [1, 2, \cdots, n]$ $\eta_{\alpha_1\cdots\alpha_d} = \left\{\bigotimes_{i=1}^{n} u_i\right\}$, and $u_{i\notin\{\alpha_1,\ldots,\alpha_d\}} = \mathbb{I}$, else, $u_i \in \{H, HS\}$. In each of these subsets $\{\eta_{\alpha_1\cdots\alpha_d}\}$, the non-identity unitaries $\{H, HS\}$ simultaneously act at d-chosen sites decided by the choices of α_k. There are total $\binom{n}{d}$ subsets $\eta_{\alpha_1\ldots\alpha_d}$ each with cardinality 2^d. The PSE $\widehat{\rho}_d$ is constructed via sampling these unitaries and the pseudo-inverse (2.1) with $p = |\zeta_d| = \binom{n}{d}\times 2^d + 1$. However, each subset $\zeta_{d\alpha}$ with identity $\{\mathbb{I}^{\otimes n}, \eta_{\alpha_1\cdots\alpha_d}\}$ for a particular choice of $\alpha_1\cdots\alpha_d$ generates the PSE $\zeta_{d\alpha}$, which estimates the d-flip terms corresponding to the qubits chosen by α_k's, with pseudo-inverse strength $p = |\zeta_{d\alpha}| = 2^d + 1$. Similarly, we can construct PSEs using different subset of ζ_d given by $\tilde{\zeta}_d = \bigcup_i \zeta_{di}$ and tuning the pseudo-inverse strength to be $p = |\tilde{\zeta}_d|$.

Chapter 3

PQST for Structured Operators

In this section, we present structured operators where PQST enables efficient estimation. PQST is particularly useful when either the density matrix or the observable exhibits a specific structure, as demonstrated in

3.1 X Shadow Tomography

If the observable has an X-structure, the expectation value can be determined using the X-shadow for any density matrix. Conversely, if the density matrix itself has an X-structure, the expectation value can be computed using the X-shadow for any observable.

X-structured operators : We can use the X-shadow which samples unitaries uniformly from ζ_X to compute the expectation of observables of the form given by

$$\mathcal{P} = \mathcal{P}_Z + \mathcal{P}_{XY}, \tag{3.1}$$

where $\mathcal{P}_Z$ and $\mathcal{P}_{XY}$ can be any linear combinations of Pauli strings made of $\{\mathbb{I}, Z\}$ and $\{X, Y\}$ operators respectively. Note that $\mathcal{P}$ is a X-structured operator, i.e., contains only diagonal and anti-diagonal elements in the computational basis for the n qubits.

Many operators representing Hamiltonians of commonly studied systems such as trans-

verse field Ising model as well as XXZ and XYZ models with longitudinal field contain X-structured operators of every adjacent pair of qubits. Thus their expectation values can be estimated efficiently using the X-tomography on every adjacent pair. This reduces the cost of unitary sampling while still capturing relevant correlations in XX, YY, and XY interactions.

In cases where the observable $\mathcal{O}$ does not have the X-structure, we can still estimate the expectation of such observables via a unitary transformation $\mathcal{U}^\dagger$, which maps the observable $\mathcal{O}$ to an observable of the form $\mathcal{P}$ in Eq. (3.1). The expectation value of $\mathcal{O}$ can then be calculated as the expectation value of the X-structured operator $\mathcal{P}$ of the rotated state $\mathcal{U}\rho\mathcal{U}^\dagger$.

$$\mathcal{O} = \mathcal{U}^\dagger \mathcal{P} \mathcal{U}. \tag{3.2}$$

Single-qubit unitaries can be implemented efficiently and with high fidelities, enlarging the set of operators whose expectation values can be estimated using X-shadow tomography. For examples, 2-qubit observables $Z \otimes X$, $Z \otimes Y$ are not directly accessible but they can be estimated by employing X-shadow tomography on $\mathcal{U}\rho\mathcal{U}^\dagger$ state, where $\mathcal{U} = \mathbb{I} \otimes H$, $\mathcal{U} = \mathbb{I} \otimes HSH$ respectively, effectively calculating X-shadow of $Z \otimes Z$ w.r.t. the rotated state in each cases.

X-structured density matrices : X-tomography can be used also to estimate the expectation values of arbitrary operators on states whose density matrix is known to be X-structured. Such states with X-structured density matrices include Werner states and Bell diagonal states (convex sums of Bell states) etc.

3.2 Non-X shadow tomography

In cases where the state or observable do not have X-structure, we can sample unitaries from smaller subsets $\{\zeta_d\}$ to extract relevant elements to estimate certain observables. As an example, see Fig 2.3, we can determine all the elements given by Ω_a from set ζ_{1a} which consists of only 3 unitaries. Similarly, if we need to estimate a combination of terms like Φ_a and Ω_b, then we can sample from subsets ζ_{2a} and ζ_{1b}, respectively and construct the PSEs

$\widehat{\rho}_{2a}$ and $\widehat{\rho}_{1b}$ separately and estimate all the Φ_a and Ω_b terms. Since this approach samples unitaries from subsets of tomographically complete sets, it is advantageous in comparison to performing full shadow tomography, which is demonstrated in Sec. 4.

Chapter 4

Numerical Analysis of PQST

We analyze the performance of PQST as a function of the number of measurements, for different structures of the observable or the state. We then compare PQST with standard QST based on unitary 2-design Clifford sampling, unitary 1-design Pauli sampling, and measurements utilizing mutually unbiased bases (MUBs) [33]. We evaluate the Mean Squared Error (MSE) $\sigma^2_{\mathcal{O}}$ of the expectation values estimated using the PSE $\widehat{\rho}$ (generated by different methods) relative to the true expectation value, given by

$$\sigma^2_{\mathcal{O}} = \frac{1}{N}\sum_{i=1}^{N}(\mathrm{Tr}(\mathcal{O}\widehat{\rho}_i) - \mathrm{Tr}(\mathcal{O}\rho))^2 \tag{4.1}$$

The results are shown in Fig. 4.1 (a-f). PQST achieves an equal/ improved scaling of variance with the number of measurements, compared to the standard QST using Clifford sampling, Pauli basis sampling, MUB sampling of unitaries, thus offering lower error bounds. This scaling behavior has been observed for arbitrary choices of density matrices and Pauli string observables that belong to respective classes, however, we have considered three cases of randomly generated density matrices separately for a 2-qubit system and a 3-qubit system. A key feature of PQST is that it samples single-qubit unitaries, which are easier to implement in near-term quantum devices from a smaller subset of a tomographically complete set while achieving improved scaling. In certain cases, PQST even outperforms the QST using Clifford, MUB sampling, based on the specific structure of the density matrices as seen for the case of X-structured density matrices in Fig 4.1 (c,f).

For our numerical simulations we have generated 2-qubit, and 3-qubit random states for a

given X-structured observable (Fig. 4.1 (a,d)) of the form in Eq. (3.1) as well as for non-X structured observable containing only single-active terms for 2-qubit case (Fig. 4.1 (b)), and non-X structured observable containing only double-active terms for 3-qubit (Fig. 4.1 (e)) case. For X-states we generate density matrices having X-structure for 2-qubit (Fig. 4.1 (c)) and 3-qubit (Fig. 4.1 (f)) systems, where we take the observable to be an arbitrary Pauli string operator. The variance is computed over $N = 1000$ independent trials for each sampling size.

4.1 Numerical details

In our numerical simulations in Sec. 4, we consider randomly generated two- and three-qubit states to verify MSE ($\sigma^2_{\mathcal{O}}$) scaling with number of measurements across different observables. Specifically, we use:

1. A two-qubit state ρ_2 to analyze MSE scaling in X-type (O_{2X}) and Non-X-type (O_{2NX}) observables.

2. A two-qubit X-state ρ_{2X} to study MSE scaling for an arbitrary observable O_2.

3. A three-qubit state ρ_3 to examine MSE scaling in X-type (O_{3X}) and Non-X-type (O_{3NX}) observables.

4. A three-qubit X-state ρ_{3X} to evaluate MSE scaling for an arbitrary observable O_3.

This structured approach systematically compares MSE scaling behaviors across different structured states and observable types.

$$\rho_2 = \begin{pmatrix} 0.3484 & 0.0242 + 0.1014i & 0.0118 - 0.0301i & -0.1986 + 0.0933i \\ 0.0242 - 0.1014i & 0.2641 & 0.0447 - 0.0050i & -0.0548 - 0.0516i \\ 0.0118 + 0.0301i & 0.0447 + 0.0050i & 0.1210 & 0.0263 - 0.0367i \\ -0.1986 - 0.0933i & -0.0548 + 0.0516i & 0.0263 + 0.0367i & 0.2665 \end{pmatrix} \tag{4.2}$$

$$\rho_{2X} = \begin{pmatrix} 0.19375 & 0 & 0 & 0.09375 \\ 0 & 0.30625 & -0.20625 & 0 \\ 0 & -0.20625 & 0.30625 & 0 \\ 0.09375 & 0 & 0 & 0.19375 \end{pmatrix} \tag{4.3}$$

$$\rho_3 = \begin{pmatrix} 0.1855 & -0.0429+0.0097i & 0.0075-0.0288i & 0.0319-0.0305i & -0.0640-0.0150i & 0.0061+0.0318i & -0.0125-0.0371i & 0.0348-0.0563i \\ -0.0429-0.0097i & 0.1172 & 0.0383+0.0321i & 0.0171-0.0024i & 0.0434-0.0252i & 0.0786-0.0181i & -0.0078+0.0359i & -0.0350+0.0078i \\ 0.0075+0.0288i & 0.0383-0.0321i & 0.1012 & 0.0545-0.0414i & 0.0106-0.0673i & 0.0505-0.0307i & 0.0487-0.0143i & -0.0449+0.0372i \\ 0.0319+0.0305i & 0.0171+0.0024i & 0.0545+0.0414i & 0.0957 & 0.0118-0.0219i & 0.0630+0.0153i & 0.0474-0.0341i & -0.0510+0.0032i \\ -0.0640+0.0150i & 0.0434+0.0252i & 0.0106+0.0673i & 0.0118+0.0219i & 0.1038 & 0.0349+0.0267i & -0.0042+0.0408i & -0.0387-0.0013i \\ 0.0061-0.0318i & 0.0786+0.0181i & 0.0505+0.0307i & 0.0630-0.0153i & 0.0349-0.0267i & 0.1308 & 0.0294-0.0356i & -0.0518+0.0164i \\ -0.0125+0.0371i & -0.0078-0.0359i & 0.0487+0.0143i & 0.0474+0.0341i & -0.0042-0.0408i & 0.0294+0.0356i & 0.1359 & -0.0453+0.0288i \\ 0.0348+0.0563i & -0.0350-0.0078i & -0.0449-0.0372i & -0.0510-0.0032i & -0.0387+0.0013i & -0.0518-0.0164i & -0.0453-0.0288i & 0.1300 \end{pmatrix} \tag{4.4}$$

$$\rho_{3X} = \begin{pmatrix} 0.20 & 0 & 0 & 0 & 0 & 0 & 0 & 0.05+0.02i \\ 0 & 0.15 & 0 & 0 & 0 & 0 & 0.04+0.03i & 0 \\ 0 & 0 & 0.10 & 0 & 0 & 0.03+0.01i & 0 & 0 \\ 0 & 0 & 0 & 0.18 & 0.06+0.02i & 0 & 0 & 0 \\ 0 & 0 & 0 & 0.06-0.02i & 0.12 & 0 & 0 & 0 \\ 0 & 0 & 0.03-0.01i & 0 & 0 & 0.10 & 0 & 0 \\ 0 & 0.04-0.03i & 0 & 0 & 0 & 0 & 0.08 & 0 \\ 0.05-0.02i & 0 & 0 & 0 & 0 & 0 & 0 & 0.07 \end{pmatrix} \tag{4.5}$$

The observables whose expectation values we have calculated are listed below-

1. $O_{2X} = 8ZZ + 2XY + 3XX - 10\ \mathbb{I}Z$ with spectral norm $||O_{2X}|| = 18.630$
2. $O_{2NX} = 7XZ + 15YZ + 12ZX$ with spectral norm $||O_{2NX}|| = 28.553$
3. $O_2 = 8ZY + 12XZ + 3XX - 10\ \mathbb{I}Z + 9\ \mathbb{I}\mathbb{I}$ with spectral norm $||O_2|| = 34.061$
4. $O_{3X} = 2\ \mathbb{I}\mathbb{I}Z + 4XXX + 6XYX + 8YYX + 10\ \mathbb{I}ZZ + 12XXX$ with spectral norm $||O_{3X}|| = 34.819$

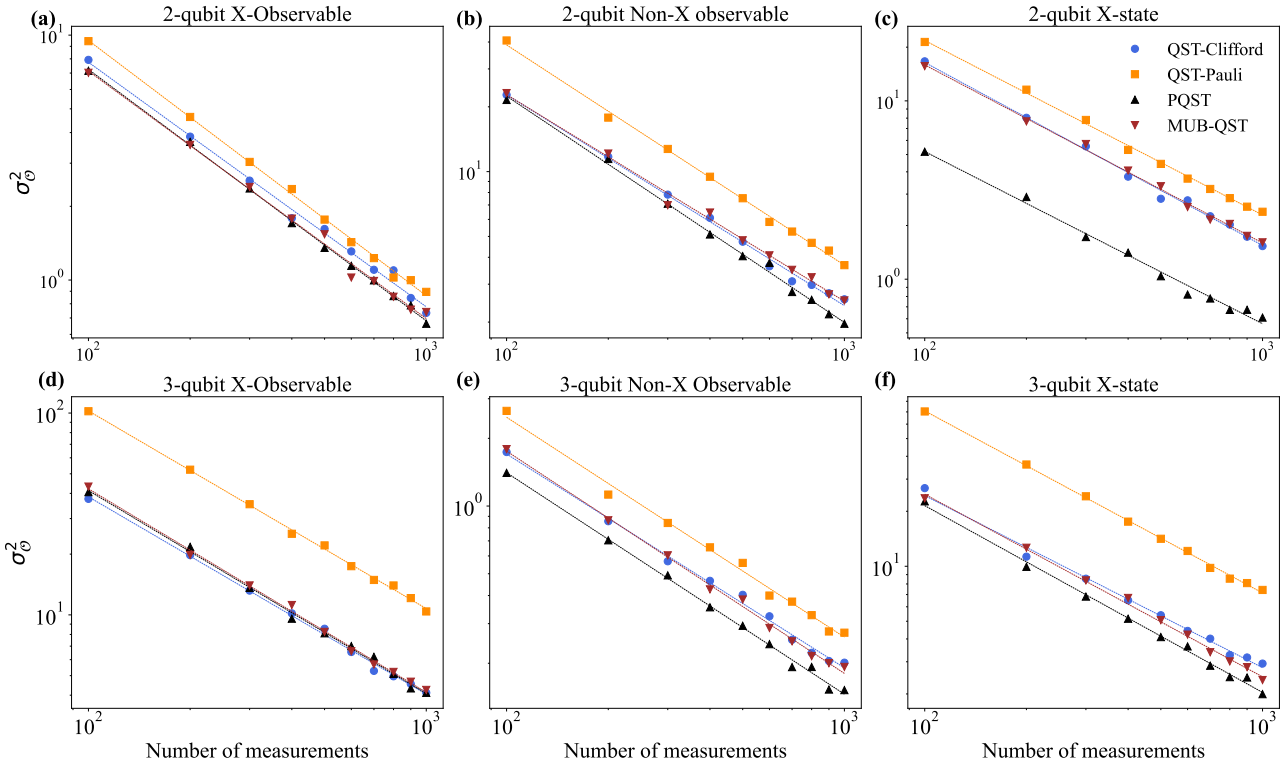

Figure 4.1: The scaling of variance, $\sigma_{\mathcal{O}}^2$ with the number of measurements is analyzed for different scenarios. We consider an X-type structured observable with a randomly generated quantum state for a 2-qubit system in case (a) and for a 3-qubit system in case (d). Similarly, a non-X-type observable with a randomly generated quantum state is examined for a 2-qubit system in case (b) and for a 3-qubit system in case (e). Additionally, we study the scaling behavior for a 2-qubit X-state with an arbitrarily chosen Pauli string observable in case (c) and extend this analysis to a 3-qubit X-state in case (f).

5. $O_{3NX} = 2XZY + 4Y\mathbb{I}Y$ with spectral norm $||O_{3NX}|| = 4.472$

6. $O_3 = 5XXX + 10ZZZ + 7XYY - 6Z\mathbb{I}Z + 6YYY + 7ZXX - 2ZX\mathbb{I}$ with spectral norm $||O_3|| = 25.0381$

Chapter 5

Experimental Demonstration with NMR

5.1 Nuclear magnetic resonance

Nuclear Magnetic Resonance (NMR) is a powerful analytical technique widely used in chemistry and physics to determine molecular structures, study molecular dynamics, and analyze complex mixtures. In recent years, NMR has also emerged as a near-term quantum device, playing a significant role in Quantum Information Processing (QIP). The fundamental principle of NMR relies on the interaction between nuclear spins and an external magnetic field, leading to energy level splitting due to the Zeeman effect. The energy levels for a nucleus with spin quantum number I are given by:

$$E_m = -\gamma \hbar m B_0, \tag{5.1}$$

where B_0 represents the externally applied magnetic field, γ is the gyromagnetic ratio of the nucleus, $\hbar$ is the reduced Planck's constant, and m is the magnetic quantum number, which takes values from $\{-I, -I+1, \ldots, I-1, I\}$. The corresponding resonance frequency, known as the *Larmor frequency*, is given by:

$$\omega_0 = \gamma B_0. \tag{5.2}$$

NMR-active nuclei must have a nonzero spin quantum number ($I \neq 0$). For quantum computing applications, we often use nuclei with $I = \frac{1}{2}$, as they provide a well-defined two-level quantum system suitable for qubit representation.

5.1.1 Qubit Representation and Internal Hamiltonian

In an NMR system, a single qubit is represented by a spin-$\frac{1}{2}$ nucleus. The internal Hamiltonian for such a system is given by:

$$H_0 = -\hbar\omega_0 I_z, \tag{5.3}$$

where $I_z = \frac{\sigma_z}{2}$, demonstrating its equivalence to a two-level quantum system.

For an n-qubit system composed of n coupled spin-$\frac{1}{2}$ nuclei, the internal Hamiltonian takes the form [25]:

$$H_0 = -\sum_{i=1}^{n} \hbar\omega_i I_z^i + 2\pi\hbar \sum_{i<j} J_{ij} I_z^i \cdot I_z^j, \tag{5.4}$$

where J_{ij} represents the scalar coupling between the nuclei, and ω_i is the Larmor frequency of the i-th nucleus. Under the weak coupling approximation, where $|J_{ij}| \ll |\omega_i - \omega_j|$, the Hamiltonian simplifies to the secular form:

$$H_0 = -\sum_{i=1}^{n} \hbar\omega_i I_z^i + 2\pi\hbar \sum_{i<j} J_{ij} I_z^i I_z^j. \tag{5.5}$$

5.1.2 Initialization of NMR Qubits

NMR qubits are initialized in thermal equilibrium at temperature T, where the density matrix follows the Boltzmann distribution:

$$\rho_{\text{eq}} = \frac{e^{-H_0/k_B T}}{\text{Tr}[e^{-H_0/k_B T}]}. \tag{5.6}$$

Since $E_i \ll k_B T$ at room temperature, we approximate it using a Taylor expansion:

$$\rho_{\text{eq}} \approx \frac{I}{2^n} + \sum_{i=0}^{2^n-1} \frac{\hbar\omega_{0i}}{2^n k_B T} I_z^i. \tag{5.7}$$

The first term is a scaled identity matrix, which does not contribute to the NMR signal, while the second term, known as the deviation matrix ρ_I, is the measurable part of the system. The signal strength decreases as 2^n, limiting the scalability of NMR-based quantum computing.

5.1.3 Quantum Gates in NMR

Quantum gates are implemented using radio-frequency (rf) pulses, which induce coherent spin rotations. The total Hamiltonian for a single qubit under an rf pulse is:

$$H_{\text{tot}}(t) = H_0 + H_{\text{rf}}(t) = -\hbar\omega_0 I_z - \hbar\omega_1 \left[I_x \cos(\omega_{\text{rf}} t + \phi) + I_y \sin(\omega_{\text{rf}} t + \phi) \right], \tag{5.8}$$

where $\omega_1 = \gamma B_1$ is the rf amplitude, and ϕ is the pulse phase. Transforming to the rotating frame, the effective Hamiltonian simplifies to:

$$H_e = \hbar\Omega I_z + \hbar\omega_1 \left[I_x \cos(\phi) + I_y \sin(\phi) \right], \tag{5.9}$$

where $\Omega = \omega_0 - \omega_{\text{rf}}$ is the frequency offset. Under this Hamiltonian, the qubit state evolves as:

$$\rho(\tau) = e^{-iH_e\tau} \rho(0) e^{iH_e\tau}. \tag{5.10}$$

In multi-qubit systems, the qubits interact via a coupling Hamiltonian:

$$H_{\text{int}} = 2\pi\hbar J_{12} I_z^1 I_z^2, \tag{5.11}$$

where J_{12} is the coupling constant. One can control the effective rotation angle and implement desired quantum operations by adjusting the pulse duration.

5.1.4 Pulse Shaping Techniques

Quantum gate operations typically use *hard pulses*, which have short durations and broad frequency spectra, ensuring uniform excitation of multiple qubits. However, in homonuclear systems or in cases with significant radio-frequency (RF) inhomogeneity, *soft pulses* with narrow bandwidths are preferred to address specific transitions selectively.

For precise quantum control, optimal control techniques such as *Gradient Ascent Pulse Engineering* (GRAPE) [23] are employed. These techniques optimize pulse shapes to maximize fidelity and compensate for system imperfections, ensuring high-precision quantum gate implementations.

NMR-based quantum computing relies on coherent control of nuclear spins using rf pulses. By leveraging different pulse sequences, coupling interactions, and optimal control methods, it is possible to implement high-fidelity quantum gates. Despite the challenges posed by signal decay in large systems, techniques like pseudo-pure state preparation and optimal pulse design make NMR a powerful platform for quantum information processing.

5.2 Experimental Demonstration of PQST

^1H (Hz)	^{13}C (Hz)		T_1 (s)	T_2 (s)	T_2^* (s)
0	217.715	^1H	4.88	3.5	0.68
	0	^{13}C	5.78	-	0.26

Table 5.1: Chemical shifts (diagonal elements), J-coupling constants, and relaxation times (T_1, T_2) for the $^{13}CHCl_3$ molecule in DMSO.

We now describe the experimental demonstration of PQST in a two-qubit NMR register ^{13}C-Chloroform ($CHCl_3$) wherein ^{13}C and ^{1}H spin-1/2 nuclei are qubit 1 and 2 respectively (see Fig. 5.1 (a)). In a strong $\hat{z}$-magnetic field of 11.7 T inside a Bruker 500 MHz NMR

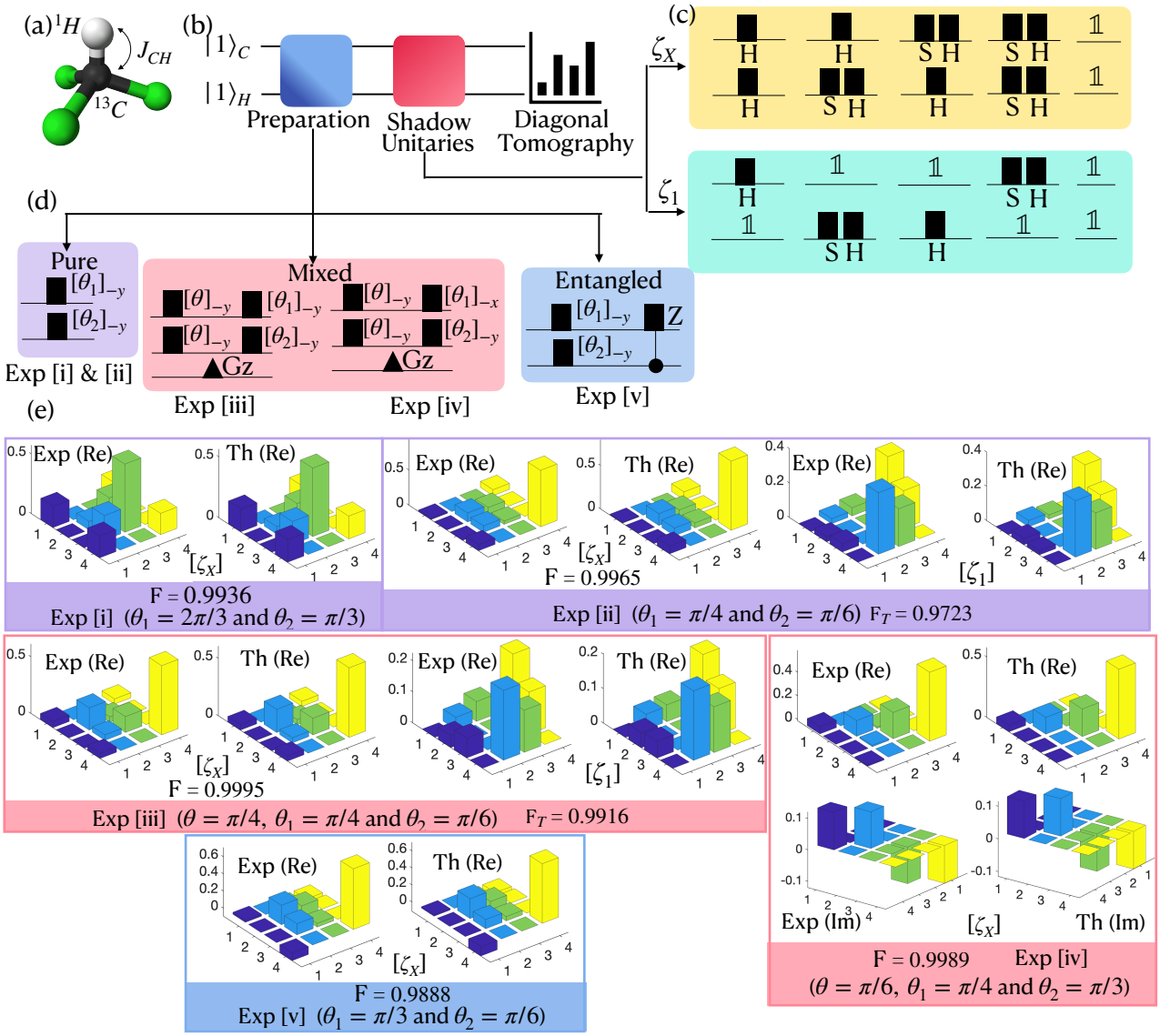

Figure 5.1: (a) The molecular structure of 13C-Chloroform with the qubits labeled. The measured relaxation times are $T_1 = 4.88s$, $T_2 = 3.5s$ and $T_2^* = 0.68s$ for ^1H, and $T_1 = 5.78s$ and $T_2^* = 0.26s$ for ^{13}C. (b) A schematic showing the three basic steps involved in partial shadow tomography experiments. First, the desired state is prepared following the pulse sequences (for more information regarding the prepared states, see Tab. 5.2) shown in (d), which is followed by the application of the shadow unitaries from set ζ_X or ζ_1 (c) depending on whether we want to do an X tomography or non-X tomography. Finally, the populations are measured in the computational basis using standard diagonal tomography. The results (e) show remarkably good fidelities achieved, considering some experimental error in the preparation and applications of shadow unitaries (F_T denotes the full state fidelity, F is the fidelity of the X-shadow).

Exp No.	State Prepared	Class	PPS purity	PPS Entanglement
Exp[i]	$\rho_i = \|\eta_{\rm i}\rangle\langle\eta_{\rm i}\|$, $\|\eta_{\rm i}\rangle = \left[\cos\left(\frac{\pi}{6}\right)\|1\rangle + \sin\left(\frac{\pi}{6}\right)\|0\rangle\right] \otimes \left[\cos\left(\frac{\pi}{3}\right)\|1\rangle + \sin\left(\frac{\pi}{3}\right)\|0\rangle\right]$	Pure	1	0
Exp[ii]	$\rho_{ii} = \|\eta_{\rm ii}\rangle\langle\eta_{\rm ii}\|$, $\|\eta_{\rm ii}\rangle = \left[\cos\left(\frac{\pi}{8}\right)\|1\rangle + \sin\left(\frac{\pi}{8}\right)\|0\rangle\right] \otimes \left[\cos\left(\frac{\pi}{12}\right)\|1\rangle + \sin\left(\frac{\pi}{12}\right)\|0\rangle\right]$	Pure	1	0
Exp[iii]	$\rho_{\rm iii} = \left[\frac{\mathbb{1}}{2} - \cos\left(\frac{\pi}{4}\right) R_1\right] \otimes \left[\frac{\mathbb{1}}{2} - \cos\left(\frac{\pi}{4}\right) R_2\right]$, $R_1 = \cos\left(\frac{\pi}{4}\right) I_z - \sin\left(\frac{\pi}{4}\right) I_x$, $R_2 = \cos\left(\frac{\pi}{6}\right) I_z - \sin\left(\frac{\pi}{6}\right) I_x$	Mixed	0.56	0
Exp[iv]	$\rho_{\rm iv} = \left[\frac{\mathbb{1}}{2} - \cos\left(\frac{\pi}{6}\right) R_3\right] \otimes \left[\frac{\mathbb{1}}{2} - \cos\left(\frac{\pi}{6}\right) R_4\right]$, $R_3 = \cos\left(\frac{\pi}{4}\right) I_z + \sin\left(\frac{\pi}{4}\right) I_y$, $R_4 = \cos\left(\frac{\pi}{3}\right) I_z + \sin\left(\frac{\pi}{3}\right) I_x$	Mixed	0.765	0
Exp[v]	$\rho_{\rm v} = \|\eta_{\rm v}\rangle\langle\eta_{\rm v}\|$, $\|\eta_{\rm v}\rangle = \sin\left(\frac{\pi}{6}\right)\sin\left(\frac{\pi}{12}\right)\|00\rangle + \sin\left(\frac{\pi}{6}\right)\cos\left(\frac{\pi}{12}\right)\|01\rangle +$ $\sin\left(\frac{\pi}{12}\right)\cos\left(\frac{\pi}{6}\right)\|10\rangle - \cos\left(\frac{\pi}{6}\right)\cos\left(\frac{\pi}{12}\right)\|11\rangle$	Entangled	1	0.28

Table 5.2: List of all states prepared experimentally for testing partial shadow tomography, including their purity and entanglement values. Here, purity of a density operator ρ refers to $\mathrm{Tr}\,\rho^2$ (which is 1 for pure states and 0.25 for maximally mixed states), and entanglement is measured by usual entanglement entropy (for pure states) and by logarithmic negativity (for mixed states). Both of these measures take value 1 for maximally entangled states and 0 for separable states. The spin operator $I_k := \sigma_k/2$, where σ_k is the kth component of the Pauli operator $\vec{\sigma}$.

spectrometer, the liquid ensemble of $CHCl_3$, dissolved in Dimethyl sulfoxide (DMSO), rests in thermal equilibrium at an ambient temperature of 300 K. Under high temperature-high field assumption [5], the density matrix of the quantum register reads $\rho_{\rm th} = \mathbb{1}/4 + \epsilon(\gamma_{\rm C} I_z^{\rm C} + \gamma_{\rm H} I_z^{\rm H})$, where γ_i is the gyro-magnetic ratio of the i'th nucleus, $I_z^v := \hat{\sigma}_z^v/2$ are the spin operators, and $\epsilon \sim 10^{-5}$ is the purity factor. Using secular approximation in a doubly-rotating frame, rotating at the resonant frequency of each nucleus, the Hamiltonian can be written as [5, 25]

$$\mathcal{H}_{\rm NMR} = 2\pi\hbar J_{\rm CH} I_z^{\rm C} I_z^{\rm H}, \tag{5.12}$$

where $J_{\rm CH} = 220$ Hz is the scalar coupling constant. Starting from the thermal state $\rho_{\rm th}$, we initialize the quantum register into the pseudopure state of $|11\rangle$ [8, 13, 9]. Subsequently, using the pulses shown in Fig. 5.1 (d), we prepare each of the five different states listed in Tab. 5.2.

We now apply the shadow unitaries from the appropriate sets (ζ_X and ζ_1) as shown in Fig. 5.1 (c) and measure the populations via diagonal tomography. Being an ensemble architecture, the NMR diagonal tomography is efficient since it only requires a single readout of the NMR signal spanning over all the spin transitions after twirling non-diagonal elements and applying a detection pulse [2, 24, 30].

The experimentally measured diagonal states are back-evolved by the same shadow unitary chosen before, after which they are subjected to the pseudo-inverse (2.1) with strength parameter $p = 5$ as described in Sec. 2.5. The full estimator $\widehat{\rho}$ is constructed via combining the PSEs $\widehat{\rho_i}$ generated by respective unitary sets ζ_i. The final reconstructed states are displayed in Fig 5.1 (e) show excellent agreement with the actual states ρ, with most of the fidelities $F = \left(\text{tr}\sqrt{\sqrt{\rho}\widehat{\rho}\sqrt{\rho}}\right)^2$ being around 0.99. Such high fidelities confirm the robustness of PQST against the experimental limitations in preparing the states and applying shadow unitaries in the presence of thermal electronic noise introducing random errors and RF inhomogeneity introducing systematic errors.

5.3 Diagonal Tomography Results

In this section, we present the experimental data obtained from NMR diagonal tomography, as described in Section 5. Each quantum state is evolved under the action of unitaries U from the sets ζ_X and ζ_1, followed by population measurements via diagonal tomography, as shown in Fig. 5.2. The resulting diagonal matrices are then inverse-rotated using $U_i^\dagger$. To construct the partial state estimators (PSEs) $\widehat{\rho}_X$ and $\widehat{\rho}_1$, we apply the pseudo-inverse (2.1) with $p = |\zeta_X| = |\zeta_1| = 5$ on each of the inverse-rotated diagonally tomographed states and compute the average over all unitary choices in their respective sets. Finally, we reconstruct the full density matrix by selectively incorporating the density matrix elements that remain preserved in each of the PSEs using Eq. (2.12). The unitaries in each set are labeled in Fig. 5.2 by

$$\zeta_X = \{U_1 = H \otimes H,\ U_2 = H \otimes HS,\ U_3 = HS \otimes H,\ U_4 = HS \otimes HS,\ U_5 = \mathbb{I} \otimes \mathbb{I}\}$$

$$\zeta_1 = \{U_1 = H \otimes \mathbb{I},\ U_2 = \mathbb{I} \otimes HS,\ U_3 = \mathbb{I} \otimes H,\ U_4 = HS \otimes \mathbb{I},\ U_5 = \mathbb{I} \otimes \mathbb{I}\}.$$

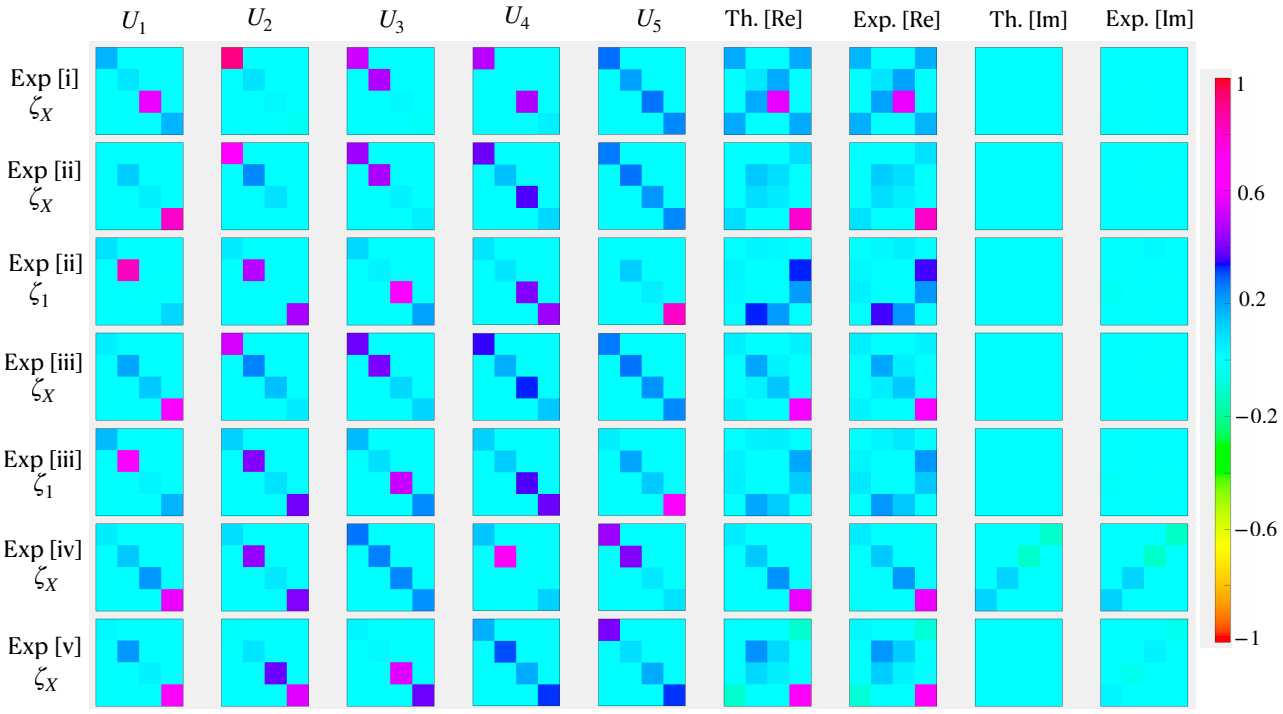

Figure 5.2: Experimental data from diagonal tomography were obtained using unitaries sampled from the sets ζ_X and ζ_1 for a two-qubit system. The specific unitaries U_i associated with each set are listed in Appendix 5.3. The full density matrix is reconstructed by combining partial information preserved in each estimator, $\widehat{\rho}_X$ and $\widehat{\rho}_1$. The theoretical and experimental values are compared in two parts: Real: Th.[Re] and Exp.[Re] and Imaginary: Th.[Im] and Exp.[Im].

Chapter 6

Conclusion

Quantum shadow tomography is a powerful tool to estimate the expectation values of both linear and nonlinear observables for an unknown quantum state. However, in many settings such as in variational quantum algorithms (VQAs) [6], we are interested in calculating specific expectation values such as that of nearest neighbor X_1X_2, Y_1Y_2, Z_1Z_2 operators in the case of a VQA to optimize the XXZ ground state. Executing the full shadow tomography protocol may be unnecessary. In scenarios where prior knowledge about the structure of required observables or the density matrix is available — for instance, from symmetries or state preparation protocols, partial quantum shadow tomography (PQST) that we introduced here can provide an efficient alternative.

We have generalized the inverse channel description with the pseudo-inverse formalism and provided a systematic approach for performing partial shadow tomography using carefully selected subsets of single-qubit unitaries. This protocol helps identify minimal sets of unitaries that, when paired with appropriate pseudo-inverses, facilitate efficient partial shadow tomography. A promising direction for future research is the exhaustive exploration of optimal combinations of subsets of tomographically complete sets of unitaries that enable partial estimation of density matrix elements. This would allow for the estimation of subsystem properties, effectively reducing the complexity of unitary sampling while enabling more efficient subsystem shadow tomography.

PQST achieves the same power law scaling of variance $\sigma^2_{\mathcal{O}}$ with the number of measurements x, $\sigma^2_{\mathcal{O}} \sim ax^{-\gamma}$ where the exponent γ is comparable to that obtained using Clifford or

mutually unbiased basis (MUB) unitary sampling. However, for specific operators, PQST achieves a smaller amplitude a of the power law, leading to a lower overall variance for the same number of measurements, as demonstrated by our numerical analysis. Additionally PQST has the advantage of relying on simple local unitaries, unlike other protocols that may require nonlocal unitaries with significantly greater circuit depth. Single-qubit unitaries are easier to implement in practice, achieve better fidelities and are noise-resistant. On account of the simplicity of the unitaries involved, our experimental implementation of PQST for the case of two NMR qubits demonstrated remarkably high fidelities. Quantum state tomography is a challenging yet essential task for advancing quantum technologies, as it enables the estimation of expectation values, characterization of quantum states, and validation of state-preparation protocols. However, when the structure of the output quantum state or observables is partially known, our method offers an efficient approach for extracting state information. We believe this work will inspire further research into more sophisticated and optimized state estimation techniques that leverage partial prior knowledge.

Appendix A

Haar measure and Unitary k-designs

The Haar measure on the unitary group $U(d)$ is the unique probability measure μ_H that is both left and right invariant over the group $U(d)$. That is, for all integrable functions f and for all $V \in U(d)$, we have:

$$\int_{U(d)} f(U) d\mu_H(U) = \int_{U(d)} f(UV) d\mu_H(U) = \int_{U(d)} f(VU) d\mu_H(U). \tag{A.1}$$

This can be rewritten as the expected value of $f(U)$ with respect to the probability measure μ_H, denoted as:

$$\mathbb{E}_{U \sim \mu_H}[f(U)] := \int U(d) f(U) d\mu_H(U). \tag{A.2}$$

A.1 The k-th Moment Operator

The k-th moment operator, with respect to the probability measure μ_H, is defined as:

$$M_{\mu_H}^{(k)} : L(\mathbb{C}^d)^{\otimes k} \to L(\mathbb{C}^d)^{\otimes k}, \tag{A.3}$$

given by:

$$M_{\mu_H}^{(k)}(O) := \mathbb{E}_{U\sim\mu_H}\left[U^{\otimes k} O U^{\dagger\otimes k}\right], \tag{A.4}$$

for all operators $O \in L(\mathbb{C}^d)^{\otimes k}$.

A.2 Properties

- Any statistical property of a Haar-random unitary does not depend on its specific choice.
- Haar-random unitaries are hard to sample exactly but can be approximated using random quantum circuits.
- The expectation of an observable O under Haar measure satisfies:

$$\mathbb{E}_U[UOU^\dagger] = \frac{\mathrm{Tr}(O)}{d}\mathbb{I}_d, \tag{A.5}$$

  which describes how Haar-random unitaries scramble operators.

A.3 Unitary k-Designs

A unitary k-design is a finite set of unitary operators that mimics the statistical properties of Haar-random unitaries up to the k-th moment.

A.4 Definition

Let ν be a probability distribution defined over a set of unitaries $S \subseteq U(d)$. The distribution ν is a unitary k-design if and only if:

$$\mathbb{E}_{V\sim\nu}\left[V^{\otimes k} O V^{\dagger\otimes k}\right] = \mathbb{E}_{U\sim\mu_H}\left[U^{\otimes k} O U^{\dagger\otimes k}\right], \tag{A.6}$$

for all $O \in L(\mathbb{C}^d)^{\otimes k}$.

A.5 Properties

- A **1-design** reproduces uniform averaging over quantum states.
- A **2-design** captures second-moment statistics, making it useful for applications like *quantum state tomography* and *randomized benchmarking*.
- The **Clifford group** forms an exact **2-design** but not a **3-design**.
- Haar-random unitaries are perfect **∞-designs**, but implementing them requires exponential resources.

Appendix B

Depolarization Channel

The Quantum depolarization channel map $\mathcal{D}$ is a quantum channel which corresponds to the convex sum of the quantum state ρ with the maximally mixed state $\mathbb{I}/2^n$ given by

$$\mathcal{D}(\rho) = (1-\lambda)\rho + \lambda\frac{\mathbb{I}}{2^n}, \tag{B.1}$$

where λ is the loss parameter. This is a completely positive tracing preserving (CPTP) map. Geometrically, this channel can be interpreted as a uniform contraction of the Bloch sphere, parameterized by λ. For a single-qubit system, the depolarization channel is represented in the form of Kraus operator representation.

$$\mathcal{D}(\rho) = \sum_{i=0}^{3} K_i \rho K_i^\dagger \tag{B.2}$$

where the K_i are defined as

$$\begin{aligned} K_0 &= \sqrt{1-\frac{3\lambda}{4}}\mathbb{I} \\ K_1 &= \sqrt{\frac{\lambda}{4}}X \\ K_2 &= \sqrt{\frac{\lambda}{4}}Y \\ K_3 &= \sqrt{\frac{\lambda}{4}}Z. \end{aligned} \tag{B.3}$$

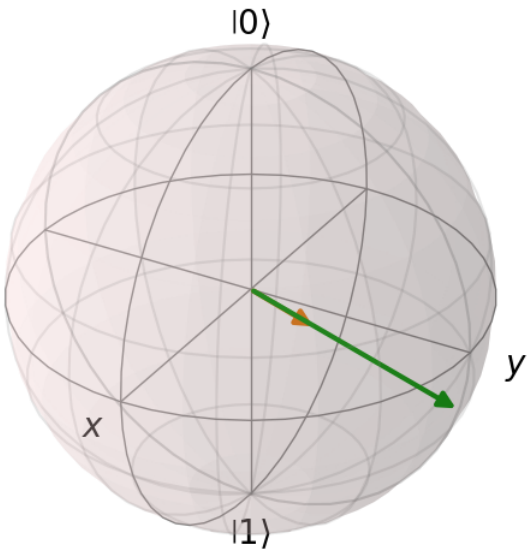

Figure B.1: Pictoral representation of a single-qubit depolarization channel (Orange arrow) on Bloch sphere for a given state (Green arrow). The depolarization channel is a unique channel that mixes Identity (maximally mixed state) and the state itself- more precisely it corresponds to uniform shrinkage of the Bloch sphere, however, preserving the information in the direction of the given state.

We have represented the depolarization channel for a single-qubit system in the Fig. B.1:

Appendix C

Channel description for the 2-qubit system

The forward channel $\mathcal{E}_d$ map generated by unitaries $\{U\}$ sampled uniformly from the unitary set ζ_d is given by:

$$\mathcal{E}_d = \mathbb{E}_{U\in\zeta_d,\hat{k}} U^\dagger \left|\hat{k}\right\rangle\!\left\langle\hat{k}\right| U \xrightarrow[\text{Measurements}]{\text{Large}} \mathbb{E}_U \left[\sum_k \langle k|U\rho U^\dagger|k\rangle\, U^\dagger|k\rangle\langle k|\, U\right], \tag{C.1}$$

where $\left|\hat{k}\right\rangle$ are the post-measurement collapsed states, $|k\rangle$ are the computational basis and $\mathbb{E}[.]$ is the empirical average. The empirical average over a unitary set ζ is computed as $\frac{1}{|\zeta|}\sum_{U_i\in\zeta} f(U_i)$, where $|\zeta|$ denotes the cardinality of the set. In the following, we have stated the results for 2-qubit system in the limit of large measurements. We will consider the sets ζ_X and ζ_1 as described in Sec. 2.5. The pseudo-inverse map action Eq. (2.1) with $p = 5$ on each of the forward channel $\mathcal{E}_X$ and $\mathcal{E}_1$ generated by uniform sampling of unitaries from set ζ_X and ζ_1, respectively is given below.

$$\widehat{\rho}_X = \mathcal{M}_5^{-1}(\mathcal{E}_X) = \begin{pmatrix} \rho_{00,00} & \rho_{00,01}+\rho_{10,11} & \rho_{00,10}+\rho_{01,11} & \rho_{11,11} \\ \rho_{01,00}+\rho_{11,10} & \rho_{01,01} & \rho_{01,10} & \rho_{01,11}+\rho_{00,10} \\ \rho_{10,00}+\rho_{11,01} & \rho_{10,01} & \rho_{10,10} & \rho_{10,11}+\rho_{00,01} \\ \rho_{00,11} & \rho_{11,01}+\rho_{10,00} & \rho_{11,10}+\rho_{01,00} & \rho_{11,11} \end{pmatrix} \tag{C.2}$$

$$\widehat{\rho}_1 = \mathcal{M}_5^{-1}(\mathcal{E}_1) = \begin{pmatrix} 2\rho_{00,00} - \rho_{11,11} & \rho_{00,01} & \rho_{00,10} & 0 \\ \rho_{01,00} & 2\rho_{01,01} - \rho_{10,10} & 0 & \rho_{01,11} \\ \rho_{10,00} & 0 & 2\rho_{10,10} - \rho_{01,01} & \rho_{10,11} \\ 0 & \rho_{11,01} & \rho_{11,10} & 2\rho_{11,11} - \rho_{00,00} \end{pmatrix} \tag{C.3}$$

The equations (C.2) and (C.3) show the extraction of subsets of elements of the full density matrix. However, if we construct PSEs using subsets of ζ_{1a} and ζ_{1b} using the pseudo-inverse in Eq. (2.1) with $p = 3$ for this case, we get the following matrices:

$$\widehat{\rho}_{1a} = \mathcal{M}_3^{-1}(\mathcal{E}_{1a}) = \begin{pmatrix} -1 + 2\rho_{00,00} + \rho_{10,10} & 0 & \rho_{00,10} & 0 \\ 0 & -1 + 2\rho_{01,01} + \rho_{11,11} & 0 & \rho_{01,11} \\ \rho_{10,00} & 0 & -1 + 2\rho_{10,10} + \rho_{00,00} & \\ 0 & \rho_{11,01} & 0 & -1 + 2\rho_{11,11} + \rho_{01,01} \end{pmatrix} \tag{C.4}$$

$$\widehat{\rho}_{1b} = \mathcal{M}_3^{-1}(\mathcal{E}_{1b}) = \begin{pmatrix} -1 + 2\rho_{00,00} + \rho_{10,10} & \rho_{00,01} & 0 & 0 \\ \rho_{01,00} & -1 + 2\rho_{01,01} + \rho_{00,00} & 0 & 0 \\ 0 & 0 & -1 + 2\rho_{10,10} + \rho_{11,11} & \rho_{10,11} \\ 0 & 0 & \rho_{11,10} & -1 + 2\rho_{11,11} + \rho_{10,10} \end{pmatrix} \tag{C.5}$$

The shadow estimator $\widehat{\rho}_{H\otimes H}$ is given below

$$\widehat{\rho}_{H\otimes H} = -\mathbb{I} + \frac{p}{4}\mathcal{B}_H \tag{C.6}$$

$$\mathcal{B}_H = \begin{pmatrix} \rho_{00,00}+\rho_{01,01} & \rho_{00,01}+\rho_{01,00} & \rho_{00,10}+\rho_{01,11} & \rho_{00,11}+\rho_{01,10} \\ +\rho_{10,10}+\rho_{11,11} & +\rho_{10,11}+\rho_{11,10} & +\rho_{10,00}+\rho_{11,01} & +\rho_{10,01}+\rho_{11,00} \\ \rho_{00,01}+\rho_{01,00} & \rho_{00,00}+\rho_{01,01} & \rho_{00,11}+\rho_{01,10} & \rho_{00,10}+\rho_{01,11} \\ +\rho_{10,11}+\rho_{11,10} & +\rho_{10,10}+\rho_{11,11} & +\rho_{10,01}+\rho_{11,00} & +\rho_{10,00}+\rho_{11,01} \\ \rho_{00,10}+\rho_{01,11} & \rho_{00,11}+\rho_{01,10} & \rho_{00,00}+\rho_{01,01} & \rho_{00,01}+\rho_{01,00} \\ +\rho_{10,00}+\rho_{11,01} & +\rho_{10,01}+\rho_{11,00} & +\rho_{10,10}+\rho_{11,11} & +\rho_{10,11}+\rho_{11,10} \\ \rho_{00,11}+\rho_{01,10} & \rho_{00,10}+\rho_{01,11} & \rho_{00,01}+\rho_{01,00} & \rho_{00,00}+\rho_{01,01} \\ +\rho_{10,01}+\rho_{11,00} & +\rho_{10,00}+\rho_{11,01} & +\rho_{10,11}+\rho_{11,10} & +\rho_{10,10}+\rho_{11,11} \end{pmatrix} \tag{C.7}$$

The shadow estimator $\widehat{\rho}_{HS\otimes HS}$ is given below

$$\widehat{\rho}_{HS\otimes HS} = -\mathbb{I} + \frac{p}{4}\mathcal{B}_{HS} \tag{C.8}$$

$$\mathcal{B}_{HS} = \begin{pmatrix} \rho_{00,00}+\rho_{01,01} & \rho_{00,01}-\rho_{01,00} & \rho_{00,10}+\rho_{01,11} & \rho_{00,11}-\rho_{01,10} \\ +\rho_{10,10}+\rho_{11,11} & +\rho_{10,11}-\rho_{11,10} & -\rho_{10,00}-\rho_{11,01} & -\rho_{10,01}+\rho_{11,00} \\ -\rho_{00,01}+\rho_{01,00} & \rho_{00,00}+\rho_{01,01} & -\rho_{00,11}+\rho_{01,10} & \rho_{00,10}+\rho_{01,11} \\ -\rho_{10,11}+\rho_{11,10} & +\rho_{10,10}+\rho_{11,11} & +\rho_{10,01}-\rho_{11,00} & -\rho_{10,00}-\rho_{11,01} \\ -\rho_{00,10}-\rho_{01,11} & -\rho_{00,11}+\rho_{01,10} & \rho_{00,00}+\rho_{01,01} & \rho_{00,01}-\rho_{01,00} \\ +\rho_{10,00}+\rho_{11,01} & +\rho_{10,01}-\rho_{11,00} & +\rho_{10,10}+\rho_{11,11} & +\rho_{10,11}-\rho_{11,10} \\ \rho_{00,11}-\rho_{01,10} & -\rho_{00,10}-\rho_{01,11} & -\rho_{00,01}+\rho_{01,00} & \rho_{00,00}+\rho_{01,01} \\ -\rho_{10,01}+\rho_{11,00} & +\rho_{10,00}+\rho_{11,01} & -\rho_{10,11}+\rho_{11,10} & +\rho_{10,10}+\rho_{11,11} \end{pmatrix} \tag{C.9}$$

Appendix D

Ancilla Assisted Shadow Tomography

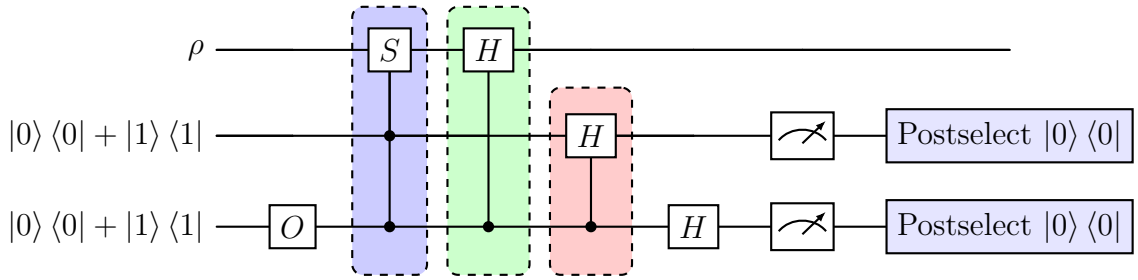

Action of O:

$$O(|0\rangle\langle 0| + |1\rangle\langle 1|)O^\dagger \to a^2 |0\rangle\langle 0| + b^2 |1\rangle\langle 1|$$

$$O = \begin{bmatrix} a & 0 \\ 0 & b \end{bmatrix} \qquad (a^2 + b^2 = 1)$$

Conditional S:

$$\mathcal{C}_S = S \otimes |0\rangle\langle 0| \otimes |0\rangle\langle 0| + I \otimes |1\rangle\langle 1| \otimes |0\rangle\langle 0| + I \otimes |0\rangle\langle 0| \otimes |1\rangle\langle 1| + I \otimes |1\rangle\langle 1| \otimes |1\rangle\langle 1|$$

Conditional H (Green):

$$\mathcal{C}_H = H \otimes I \otimes |0\rangle\langle 0| + I \otimes I \otimes |1\rangle\langle 1|$$

Conditional H (Red):

$$\mathcal{C}'_H = I \otimes H \otimes |0\rangle\langle 0| + I \otimes I \otimes |1\rangle\langle 1|$$

Circuit details:

$$\text{Initial State} : \rho \otimes [|0\rangle\langle 0| + |1\rangle\langle 1|] \otimes [|0\rangle\langle 0| + |1\rangle\langle 1|]$$

Action O on 3rd qubit:

$$\tilde{\rho} : \rho \otimes [|0\rangle\langle 0| + |1\rangle\langle 1|] \otimes [a^2 |0\rangle\langle 0| + b^2 |1\rangle\langle 1|]$$

Action of C_S:

$$\rho' = C_S \tilde{\rho} C_S^\dagger : (S\rho S \otimes |0\rangle\langle 0| + \rho \otimes |1\rangle\langle 1|) \otimes a^2 |0\rangle\langle 0| + \rho \otimes [|0\rangle\langle 0| + |1\rangle\langle 1|] \otimes b^2 |1\rangle\langle 1|$$

Action of H (Green):

$$\rho'' = C_H \rho' C_H^\dagger : (HS\rho SH \otimes |0\rangle\langle 0| + H\rho H \otimes |1\rangle\langle 1|) \otimes a^2 |0\rangle\langle 0| + \rho \otimes [|0\rangle\langle 0| + |1\rangle\langle 1|] \otimes b^2 |1\rangle\langle 1|$$

Action of H (Red):

$$\rho''' = C'_H \rho'' C'^\dagger_H : (HS\rho SH \otimes |+\rangle\langle +| + H\rho H \otimes |-\rangle\langle -|) \otimes a^2 |0\rangle\langle 0| + \rho \otimes [|+\rangle\langle +| + |-\rangle\langle -|] \otimes b^2 |1\rangle\langle 1|$$

Action of the H on the 3rd qubit:

$$\rho^{out} = (HS\rho SH \otimes |+\rangle\langle +| + H\rho H \otimes |-\rangle\langle -|) \otimes a^2 |+\rangle\langle +| + \rho \otimes [|+\rangle\langle +| + |-\rangle\langle -|] \otimes b^2 |-\rangle\langle -|$$

Post-selecting state $|0\rangle\langle 0|$ for the 3rd qubit:

$$\rho_{\text{post3}} = \frac{1}{2}[a^2(HS\rho SH \otimes |+\rangle\langle +| + H\rho H \otimes |-\rangle\langle -|) + b^2 \rho \otimes [|+\rangle\langle +| + |-\rangle\langle -|]]$$

Post-selecting state $|0\rangle\langle 0|$ for the 2nd qubit:

$$\rho_{\text{final}} = \frac{a^2}{2}(HS\rho SH + H\rho H) + b^2\rho$$

Now, let's choose the a and b values:

$$\frac{a^2}{2} = b^2$$
$$a^2 + b^2 = 1$$

we get $a = \sqrt{\frac{2}{3}}$ and $b = \sqrt{\frac{1}{3}}$

Finally we get:

$$\rho_{\text{final}} = \frac{1}{3}(HS\rho SH + H\rho H + \rho)$$

Bibliography

[1] Scott Aaronson. Shadow tomography of quantum states. *SIAM Journal on Computing*, 49(5):STOC18–368–STOC18–394, 2020. doi: 10.1137/18M120275X. URL https://doi.org/10.1137/18M120275X.

[2] Gaurav Bhole, V. S. Anjusha, and T. S. Mahesh. Steering quantum dynamics via bang-bang control: Implementing optimal fixed-point quantum search algorithm. *Phys. Rev. A*, 93:042339, Apr 2016. doi: 10.1103/PhysRevA.93.042339. URL https://link.aps.org/doi/10.1103/PhysRevA.93.042339.

[3] Kaifeng Bu, Dax Enshan Koh, Roy J. Garcia, and Arthur Jaffe. Classical shadows with pauli-invariant unitary ensembles. *npj Quantum Information*, 10(1):6, 2024. ISSN 2056-6387. doi: 10.1038/s41534-023-00801-w. URL https://doi.org/10.1038/s41534-023-00801-w.

[4] Andrea Caprotti, Joshua Morris, and Borivoje Dakić. Optimizing quantum tomography via shadow inversion. *Phys. Rev. Res.*, 6:033301, Sep 2024. doi: 10.1103/PhysRevResearch.6.033301. URL https://link.aps.org/doi/10.1103/PhysRevResearch.6.033301.

[5] John Cavanagh. *Protein NMR spectroscopy: principles and practice*. Academic press, 1996.

[6] M. Cerezo, Andrew Arrasmith, Ryan Babbush, Simon C. Benjamin, Suguru Endo, Keisuke Fujii, Jarrod R. McClean, Kosuke Mitarai, Xiao Yuan, Lukasz Cincio, and Patrick J. Coles. Variational quantum algorithms. *Nature Reviews Physics*, 3(9):625–644, Sep 2021. ISSN 2522-5820. doi: 10.1038/s42254-021-00348-9. URL https://doi.org/10.1038/s42254-021-00348-9.

[7] Senrui Chen, Wenjun Yu, Pei Zeng, and Steven T. Flammia. Robust shadow estimation. *PRX Quantum*, 2:030348, Sep 2021. doi: 10.1103/PRXQuantum.2.030348. URL https://link.aps.org/doi/10.1103/PRXQuantum.2.030348.

[8] David G Cory, Amr F Fahmy, and Timothy F Havel. Ensemble quantum computing by nmr spectroscopy. *Proceedings of the National Academy of Sciences*, 94(5):1634–1639, 1997. doi: 10.1073/pnas.94.5.1634. URL https://doi.org/10.1073/pnas.94.5.1634.

[9] David G Cory, Mark D Price, and Timothy F Havel. Nuclear magnetic resonance spectroscopy: An experimentally accessible paradigm for quantum computing. *Physica D: Nonlinear Phenomena*, 120(1-2):82–101, 1998. doi: 10.1016/S0167-2789(98)00046-3. URL https://doi.org/10.1016/S0167-2789(98)00046-3.

[10] Andreas Elben, Richard Kueng, Hsin-Yuan (Robert) Huang, Rick van Bijnen, Christian Kokail, Marcello Dalmonte, Pasquale Calabrese, Barbara Kraus, John Preskill, Peter Zoller, and Benoît Vermersch. Mixed-state entanglement from local randomized measurements. *Phys. Rev. Lett.*, 125:200501, Nov 2020. doi: 10.1103/PhysRevLett.125.200501. URL https://link.aps.org/doi/10.1103/PhysRevLett.125.200501.

[11] Andreas Elben, Steven T. Flammia, Hsin-Yuan Huang, Richard Kueng, John Preskill, Benoît Vermersch, and Peter Zoller. The randomized measurement toolbox. *Nature Reviews Physics*, 5(1):9–24, 2023. doi: 10.1038/s42254-022-00535-2. URL https://doi.org/10.1038/s42254-022-00535-2.

[12] Roy J. Garcia, You Zhou, and Arthur Jaffe. Quantum scrambling with classical shadows. *Phys. Rev. Res.*, 3:033155, Aug 2021. doi: 10.1103/PhysRevResearch.3.033155. URL https://link.aps.org/doi/10.1103/PhysRevResearch.3.033155.

[13] Neil A Gershenfeld and Isaac L Chuang. Bulk spin-resonance quantum computation. *science*, 275(5298):350–356, 1997. doi: 10.1126/science.275.5298.350. URL https://doi.org/10.1126/science.275.5298.350.

[14] Cho Gyungmin and Kim Dohun. Machine learning on quantum experimental data toward solving quantum many-body problems. *Nature Communications*, 15(1):7552, 2024. ISSN 2041-1723. doi: 10.1038/s41467-024-51932-3. URL https://doi.org/10.1038/s41467-024-51932-3.

[15] Charles Hadfield. Adaptive pauli shadows for energy estimation, 2021. URL https://arxiv.org/abs/2105.12207.

[16] Hong-Ye Hu and Yi-Zhuang You. Hamiltonian-driven shadow tomography of quantum states. *Phys. Rev. Res.*, 4:013054, Jan 2022. doi: 10.1103/PhysRevResearch.4.013054. URL https://link.aps.org/doi/10.1103/PhysRevResearch.4.013054.

[17] Hong-Ye Hu and Yi-Zhuang You. Hamiltonian-driven shadow tomography of quantum states. *Phys. Rev. Res.*, 4:013054, Jan 2022. doi: 10.1103/PhysRevResearch.4.013054. URL https://link.aps.org/doi/10.1103/PhysRevResearch.4.013054.

[18] Hong-Ye Hu, Soonwon Choi, and Yi-Zhuang You. Classical shadow tomography with locally scrambled quantum dynamics. *Phys. Rev. Res.*, 5:023027, Apr 2023. doi: 10.1103/PhysRevResearch.5.023027. URL https://link.aps.org/doi/10.1103/PhysRevResearch.5.023027.

[19] Hsin-Yuan Huang, Richard Kueng, and John Preskill. Predicting many properties of a quantum system from very few measurements. *Nature Physics*, 16(10): 1050–1057, 2020. doi: 10.1038/s41567-020-0932-7. URL https://doi.org/10.1038/s41567-020-0932-7.

[20] L. Innocenti, S. Lorenzo, I. Palmisano, F. Albarelli, A. Ferraro, M. Paternostro, and G. M. Palma. Shadow tomography on general measurement frames. *PRX Quantum*, 4:040328, Nov 2023. doi: 10.1103/PRXQuantum.4.040328. URL https://link.aps.org/doi/10.1103/PRXQuantum.4.040328.

[21] Matteo Ippoliti. Classical shadows based on locally-entangled measurements. *Quantum*, 8:1293, March 2024. ISSN 2521-327X. doi: 10.22331/q-2024-03-21-1293. URL https://doi.org/10.22331/q-2024-03-21-1293.

[22] Sofiene Jerbi, Casper Gyurik, Simon C. Marshall, Riccardo Molteni, and Vedran Dunjko. Shadows of quantum machine learning. *Nature Communications*, 15(1):5676, 2024. ISSN 2041-1723. doi: 10.1038/s41467-024-49877-8. URL https://doi.org/10.1038/s41467-024-49877-8.

[23] Navin Khaneja, Timo Reiss, Cindie Kehlet, Thomas Schulte-Herbrüggen, and Steffen J. Glaser. Optimal control of coupled spin dynamics: design of nmr pulse sequences by gradient ascent algorithms. *Journal of Magnetic Resonance*, 172(2):296–305, Feb 2005. ISSN 1090-7807. doi: 10.1016/j.jmr.2004.11.004.

[24] Jae-Seung Lee. The quantum state tomography on an nmr system. *Physics Letters A*, 305(6):349–353, 2002. ISSN 0375-9601. doi: https://doi.org/10.1016/

S0375-9601(02)01479-2. URL https://www.sciencedirect.com/science/article/pii/S0375960102014792.

[25] Malcolm H Levitt. *Spin dynamics: basics of nuclear magnetic resonance*. John Wiley & Sons, 2008.

[26] Max McGinley, Sebastian Leontica, Samuel J. Garratt, Jovan Jovanovic, and Steven H. Simon. Quantifying information scrambling via classical shadow tomography on programmable quantum simulators. *Phys. Rev. A*, 106:012441, Jul 2022. doi: 10.1103/PhysRevA.106.012441. URL https://link.aps.org/doi/10.1103/PhysRevA.106.012441.

[27] Antonio Anna Mele. Introduction to Haar Measure Tools in Quantum Information: A Beginner's Tutorial. *Quantum*, 8:1340, May 2024. ISSN 2521-327X. doi: 10.22331/q-2024-05-08-1340. URL https://doi.org/10.22331/q-2024-05-08-1340.

[28] Antoine Neven, Jose Carrasco, Vittorio Vitale, Christian Kokail, Andreas Elben, Marcello Dalmonte, Pasquale Calabrese, Peter Zoller, Benoît Vermersch, Richard Kueng, and Barbara Kraus. Symmetry-resolved entanglement detection using partial transpose moments. *npj Quantum Information*, 7(1):152, 2021. ISSN 2056-6387. doi: 10.1038/s41534-021-00487-y. URL https://doi.org/10.1038/s41534-021-00487-y.

[29] Aniket Sengupta, Arijit Chatterjee, Sreejith G. J., and T. S. Mahesh. Partial quantum shadow tomography for structured operators and its experimental demonstration using nmr, 2025. URL https://arxiv.org/abs/2503.14491.

[30] Abhishek Shukla, K. Rama Koteswara Rao, and T. S. Mahesh. Ancilla-assisted quantum state tomography in multiqubit registers. *Phys. Rev. A*, 87:062317, Jun 2013. doi: 10.1103/PhysRevA.87.062317. URL https://link.aps.org/doi/10.1103/PhysRevA.87.062317.

[31] Roman Stricker, Michael Meth, Lukas Postler, Claire Edmunds, Chris Ferrie, Rainer Blatt, Philipp Schindler, Thomas Monz, Richard Kueng, and Martin Ringbauer. Experimental single-setting quantum state tomography. *PRX Quantum*, 3:040310, Oct 2022. doi: 10.1103/PRXQuantum.3.040310. URL https://link.aps.org/doi/10.1103/PRXQuantum.3.040310.

[32] G.I. Struchalin, Ya. A. Zagorovskii, E.V. Kovlakov, S.S. Straupe, and S.P. Kulik. Experimental estimation of quantum state properties from classical shadows. *PRX*

Quantum, 2:010307, Jan 2021. doi: 10.1103/PRXQuantum.2.010307. URL https://link.aps.org/doi/10.1103/PRXQuantum.2.010307.

[33] Yu Wang and Wei Cui. Classical shadow tomography with mutually unbiased bases. *Phys. Rev. A*, 109:062406, Jun 2024. doi: 10.1103/PhysRevA.109.062406. URL https://link.aps.org/doi/10.1103/PhysRevA.109.062406.

[34] Zak Webb. The clifford group forms a unitary 3-design. *Quantum Info. Comput.*, 16 (15–16):1379–1400, November 2016. ISSN 1533-7146.

[35] Victor Wei, W. A. Coish, Pooya Ronagh, and Christine A. Muschik. Neural-shadow quantum state tomography. *Phys. Rev. Res.*, 6:023250, Jun 2024. doi: 10.1103/PhysRevResearch.6.023250. URL https://link.aps.org/doi/10.1103/PhysRevResearch.6.023250.

[36] Wang Yu and Wu Dongsheng. An efficient quantum circuit construction method for mutually unbiased bases in n-qubit systems, 2024. URL https://arxiv.org/abs/2311.11698.

[37] Andrew Zhao, Nicholas C. Rubin, and Akimasa Miyake. Fermionic partial tomography via classical shadows. *Phys. Rev. Lett.*, 127:110504, Sep 2021. doi: 10.1103/PhysRevLett.127.110504. URL https://link.aps.org/doi/10.1103/PhysRevLett.127.110504.

[38] Tian-Gang Zhou and Pengfei Zhang. Efficient Classical Shadow Tomography through Many-body Localization Dynamics. *Quantum*, 8:1467, September 2024. ISSN 2521-327X. doi: 10.22331/q-2024-09-11-1467. URL https://doi.org/10.22331/q-2024-09-11-1467.

[39] Huangjun Zhu. Multiqubit clifford groups are unitary 3-designs. *Phys. Rev. A*, 96: 062336, Dec 2017. doi: 10.1103/PhysRevA.96.062336. URL https://link.aps.org/doi/10.1103/PhysRevA.96.062336.